

Characterization of Temporarily-Captured Minimoons 2020 CD₃ by Keck Time-resolved Spectrophotometry

BRYCE T. BOLIN,^{1,2} CHRISTOFFER FREMLING,¹ TIMOTHY R. HOLT,^{3,4} MATTHEW J. HANKINS,¹
TOMÁS AHUMADA,⁵ SHREYA ANAND,⁶ VARUN BHALERAU,⁷ KEVIN B. BURDGE,¹
CHRIS M. COPPERWHEAT,⁸ MICHAEL COUGHLIN,⁹ KUNAL P. DESHMUKH,¹⁰ KISHALAY DE,¹
MANSI M. KASLIWAL,¹ ALESSANDRO MORBIDELLI,¹¹ JOSIAH N. PURDUM,¹² ROBERT QUIMBY,^{12,13}
DENNIS BODEWITS,¹⁴ CHAN-KAO CHANG,¹⁵ WING-HUEN IP,¹⁵ CHEN-YEN HSU,¹⁵ RUSS R. LAHER,²
ZHONG-YI LIN,¹⁵ CAREY M. LISSE,¹⁶ FRANK J. MASCI,² CHOW-CHOONG NGEOW,¹⁵ HANJIE TAN,¹⁵
CHENGXING ZHAI,¹⁷ RICK BURRUSS,¹⁸ RICHARD DEKANY,¹⁸ ALEXANDRE DELACROIX,¹⁸
DMITRY A. DUEV,⁶ MATTHEW GRAHAM,¹ DAVID HALE,¹⁸ SHRINIVAS R. KULKARNI,¹
THOMAS KUPFER,¹⁹ ASHISH MAHABAL,^{1,20} PRZEMYSŁAW J. MRÓZ,¹ JAMES D. NEILL,¹
REED RIDDLE,²¹ HECTOR RODRIGUEZ,²² ROGER M. SMITH,²¹ MAAYANE T. SOUMAGNAC,^{23,24}
RICHARD WALTERS,¹ LIN YAN,¹ AND JEFFRY ZOLKOWER¹⁸

- ¹*Division of Physics, Mathematics and Astronomy, California Institute of Technology, Pasadena, CA 91125, U.S.A.*
²*IPAC, Mail Code 100-22, Caltech, 1200 E. California Blvd., Pasadena, CA 91125, USA*
³*University of Southern Queensland, Computational Engineering and Science Research Centre, Queensland, Australia*
⁴*Southwest Research Institute, Department of Space Studies, Boulder, CO-80302, USA*
⁵*Department of Astronomy, University of Maryland, College Park, MD 20742, USA*
⁶*Division of Physics, Mathematics and Astronomy, California Institute of Technology, Pasadena, CA 91125, USA*
⁷*Department of Physics, Indian Institute of Technology Bombay, Powai, Mumbai-400076, India*
⁸*Astrophysics Research Institute Liverpool John Moores University, 146 Brownlow Hill, Liverpool L3 5RF, United Kingdom*
⁹*School of Physics and Astronomy, University of Minnesota, Minneapolis, Minnesota 55455, USA*
¹⁰*Department of Metallurgical Engineering and Materials Science, Indian Institute of Technology Bombay, Powai, Mumbai-400076, India*
¹¹*Université Côte d'Azur, Observatoire de la Côte d'Azur, CNRS, Laboratoire Lagrange, Boulevard de l'Observatoire, CS 34229, 06304 Nice cedex 4, France*
¹²*Department of Astronomy, San Diego State University, 5500 Campanile Dr, San Diego, CA 92182, U.S.A.*
¹³*Kavli Institute for the Physics and Mathematics of the Universe (WPI), The University of Tokyo Institutes for Advanced Study, The University of Tokyo, Kashiwa, Chiba 277-8583, Japan*
¹⁴*Physics Department, Leach Science Center, Auburn University, Auburn, AL 36832, U.S.A.*
¹⁵*Institute of Astronomy, National Central University, 32001, Taiwan*
¹⁶*Johns Hopkins University Applied Physics Laboratory, Laurel, MD 20723*
¹⁷*Jet Propulsion Laboratory, California Institute of Technology, 4800 Oak Grove Drive, Pasadena, CA 91109, U.S.A.*
¹⁸*Caltech Optical Observatories, California Institute of Technology, Pasadena, CA 91125, U.S.A.*
¹⁹*Kavli Institute for Theoretical Physics, University of California, Santa Barbara, CA 93106, U.S.A.*
²⁰*Center for Data Driven Discovery, California Institute of Technology, Pasadena, CA 91125, U.S.A.*
²¹*Caltech Optical Observatories, California Institute of Technology, Pasadena, CA 91125*
²²*Caltech Optical Observatories, California Institute of Technology, Pasadena, CA 91125, U.S.A.*
²³*Lawrence Berkeley National Laboratory, 1 Cyclotron Road, Berkeley, CA 94720, U.S.A.*

²⁴*Department of Particle Physics and Astrophysics, Weizmann Institute of Science, Rehovot 76100, Israel*

(Received –; Revised –; Accepted –)

Submitted to ApJL

ABSTRACT

We present rotationally-averaged visible spectrophotometry of minimoon 2020 CD₃, the second asteroid known to become temporarily captured by the Earth-Moon system’s gravitational field. The spectrophotometry was taken with Keck I/LRIS between wavelengths 434 nm and 912 nm in *B*, *g*, *V*, *R*, *I* and RG850 filters as it was leaving the Earth-Moon system on 2020 March 23 UTC. The broad-band spectrophotometry of 2020 CD₃ most closely resembles the spectra of V-type asteroids and some Lunar rock samples with a reddish slope of $\sim 18\%/100$ nm between 434 nm and 761 nm corresponding to colors of $g-r = 0.62 \pm 0.08$, $r-i = 0.21 \pm 0.06$ and an absorption band at ~ 900 nm corresponding to $i-z = -0.54 \pm 0.10$ (DeMeo et al. 2009; Isaacson et al. 2011). Combining our measured 31.9 ± 0.1 absolute magnitude with an albedo of 0.35 typical for V-type asteroids (DeMeo & Carry 2013), we determine 2020 CD₃’s size to be $\sim 1.0 \pm 0.1$ m making it the first minimoon and one of the smallest asteroids to be spectrally characterized. We use our time-series photometry to detect periodic lightcurve variations with a $< 10^{-4}$ false alarm probability corresponding to a lightcurve period of ~ 573 s and a lightcurve amplitude of ~ 1 mag implying 2020 CD₃ possesses a b/a axial ratio of ~ 2.5 . In addition, we extend the observational arc of 2020 CD₃ to 37 days between 2020 February 15 UTC and 2020 March 23 UTC. From the improved orbital solution for 2020 CD₃, we estimate its likely duration of its capture to be ~ 2 y, and we measure the non-gravitation perturbation on its orbit due to radiation pressure with an area-to-mass ratio of $6.9 \pm 2.4 \times 10^{-4}$ m²/kg implying a density of 2.1 ± 0.7 g/cm³, broadly compatible with the densities of other meter-scale asteroids (e.g., Micheli et al. 2012; Mommert et al. 2014) and Lunar rock (~ 2.4 g/cm³, Kiefer et al. 2012). We searched for pre-discovery observations of 2020 CD₃ in the ZTF archive as far back as 2018 October (Masci et al. 2019), but were unable to locate any positive detections.

Keywords: minor planets, asteroids: individual (2020 CD₃), temporarily captured orbiters, minimoons

1. INTRODUCTION

Asteroid population models predict that out of $\sim 10^9$ asteroids larger than 1 m in the steady-state near-Earth object (NEO) population (Harris & D’Abramo 2015; Schunová-Lilly et al. 2017) a small fraction, $\sim 10^{-7}$, become temporarily captured by the Earth-Moon system’s gravity every year (Granvik et al. 2012; Jedicke et al. 2018). These temporary natural satellites, or what we call “minimoons” have pre-capture orbital trajectories similar to the Earth which allow them to encounter the Earth at relatively low ~ 1 km/s speeds assisting them in their capture. However, the captured status of the minimoon is temporary due to its interaction with the gravity of the Sun and the Earth-Moon system and other massive Solar System bodies, with the vast majority of

minimoons only being gravitationally-bound the Earth-Moon system for ~ 70 - 280 days (Fedorets et al. 2017). Since they originate from the NEO population, the Earth-Moon system has a steady-state of temporarily captured minimoons with 1-2 being in orbit around the Earth at any given time with diameter ~ 1 m. Out of $\sim 22,000$ NEOs currently known¹, only ~ 5 known NEOs are in the 1 m range. Thus, due to their frequency of capture and small size, minimoons, therefore, provide the opportunity to study the smallest and most incomplete portion of the NEO population (Granvik et al. 2018). Also because of their low velocities relative to the Earth, minimoons provide excellent targets for human exploration missions (Elvis et al. 2011; Granvik 2013; Chyba et al. 2014).

Asteroids on quasi-satellite orbits that are strongly affected by the gravitational influence of the Earth-Moon system but are not gravitationally captured have been observed before, such as 2013 LX28 and (469219) Kamo‘oalewa (Sidorenko et al. 2014; de la Fuente Marcos & de la Fuente Marcos 2016). However, the previously only known example of an asteroid being truly gravitationally captured by the Earth-Moon system was 2006 RH₁₂₀ discovered by the Catalina Sky Survey in 2006 while it was being captured by the Earth-Moon system’s gravity. This first known minmoon remained in orbit around the Earth for ~ 400 days (Kwiatkowski et al. 2008) and had a diameter of ~ 3 m. Recently, the second known example of a temporarily-captured asteroid was discovered on 2020 February 15 UTC with the Catalina Sky Survey’s 1.5-meter telescope (Pruyne et al. 2020).

At the time of discovery on 2020 February 15 UTC, 2020 CD₃ had a highly eccentric geocentrically-bound orbit with a geocentric eccentricity, e_g , of 0.96, a geocentric semi-major axis, a_p , of ~ 3 Lunar distances (LD) or ~ 0.008 au, where 1 LD equals ~ 0.00257 au, and a prograde geocentric inclination i_g of 49° . The majority of space-debris or satellites of artificial origin are contained within 0.1 LD of the Earth suggesting that the distant geocentric orbit of 2020 CD₃ is of natural origin (Tingay et al. 2013). It is possible for artificial objects such as spacecraft boosters to be on more distant geocentric orbits that may have trajectories similar to temporary natural orbits, such as J002E3, a possible Apollo program-era rocket booster (Jorgensen et al. 2003). The Minor Planet Center maintains a list of known spacecraft as well as distant space debris², however none of these known spacecraft or distant space debris were associated with the trajectory of 2020 CD₃ at the time of its discovery (Pruyne et al. 2020).

While the initial orbit suggests a natural origin, determining the origin from within the Solar System is less clear. As discussed above, NEO population models describe that the minmoon population originates from the Main Belt (Granvik et al. 2017), however, another possible natural origin of minimoons is from Lunar impacts due to the typical low, ~ 1 km ejection speed of Lunar debris (Gladman et al. 1995). The orbits of Lunar debris dynamically decay after a few kyrs, though it is possible that some Lunar ejecta can be re-captured by the Earth-Moon system as minimoons due to their orbital similarity with the Earth just as for minimoons of asteroidal origin (Granvik et al. 2012). However, it is currently unknown from the dynamical circumstances of Lunar debris and temporarily captured asteroids what proportion of minimoons have an origin as the former to the latter.

In this paper, we build on the discovery of 2020 CD₃ with ground-based visible observations of 2020 CD₃ as an observational test to constrain whether 2020 CD₃ is of asteroidal or Lunar debris origin. As we will discuss below, we will use the approach of Bolin et al. (2020) to combine estimation of its taxonomic classification from spectrophotometric observations at different visible wavelengths

¹ <https://minorplanetcenter.net/iau/TheIndex.html>

² <https://minorplanetcenter.net/iau/artsats/artsats.html>

as well as its physical properties. In addition, we will use the astrometry from our observations of 2020 CD₃ to extend the orbital arc and refine the orbit of 2020 CD₃ enabling study of its dynamical evolution before, during and after its capture by the Earth-Moon system. The refined orbit enabled by our observations will also serve as an independent constraint on its origin before being captured by the Earth-moon system as well as on its physical properties and origin by comparison with the NEO population model (Morbidei et al. 2020) and estimation of non-gravitational perturbations on its orbit (Mommert et al. 2014).

2. OBSERVATIONS

We used the 10 m Keck I telescope with the Low Resolution Imaging Spectrometer (LRIS) (Oke et al. 1995; Rockosi et al. 2010) to observe 2020 CD₃ on 2020 March 23.545694 UTC to March 23.583322 UTC in imaging mode (Program ID C236, PI M. Fremling). Both the blue camera consisting of a 2 x 2K x 4K Marconi CCD array and the red camera consisting of a science grade Lawrence Berkeley National Laboratory 2K x 4K CCD array were used simultaneously. Both cameras have a spatial resolution of 0.135 arcsec/pixel and were used in 2 x 2 binning mode providing an effective resolution element size of 0.27 arcsec providing a field of view of 6' x 7.8'. The 560 nm dichroic with ~50% peak transmission was used in combination with the filters *B* ($\lambda_{\text{eff}} = 435$ nm, FWHM of 91 nm), *g* ($\lambda_{\text{eff}} = 474$ nm, FWHM of 98 nm), *V* ($\lambda_{\text{eff}} = 541$ nm, FWHM of 95 nm) filters for the blue camera. The filters *R* ($\lambda_{\text{eff}} = 628$ nm, FWHM of 119 nm), *I* ($\lambda_{\text{eff}} = 760$ nm, FWHM of 123 nm) and RG850 ($\lambda_{\text{eff}} = 912$ nm, FWHM of 128 nm), similar to the SDSS *z* filter ($\lambda_{\text{eff}} = 905$ nm, FWHM of 137 nm, Fukugita et al. 1996), were used for the red camera in total with the blue camera providing six total resolution elements between 435 nm and 912 nm³. Typical exposure times were ~120 s which were tracked non-sidally at the the ~3"/min motion of 2020 CD₃. We rotated filters and used the two cameras simultaneously to limit the effect of rotational variations on photometric measurements. At the time of our observations, 2020 CD₃ was located near R.A., Dec. = 14 20 00.3, +33 15 49.7, and had a heliocentric distance, r_h , of 1.0059 au, a geocentric distance, Δ , of 0.0128 au and a phase angle, α , of 45.4063°. During our observations, the sky plane of motion of 2020 CD₃ was ~2.5 "/m and had airmass 1.03-1.08.

Images were taken of Solar-like calibrator stars in nearby fields as 2020 CD₃ were identified using the Pan-STARRS catalog (Chambers et al. 2016; Flewelling et al. 2016). The seeing was ~0.5" and data from the CFHT Sky Probe indicated that the night was photometrically stable with less than ~0.01 magnitude variations over the course of our observations⁴. Bias and flat frames were obtained using the uniform flattening screen inside the Keck dome. The reduction of the imaging data was completed using the LPipe reduction software (Perley 2019). In total, 5 x 120 s *B* filter, 5 x 120 s *g* Filter, 5 x 120 s *V* filter images, 3 x 30 s, 3 x 60 s *R* filter images, 8 x 120 s *I* filter, and 5 x 120 s RG850 filter exposures were taken. Some images contained field stars near 2020 CD₃ which were discarded. The images were median-combined into separate composite stacks for all six filters as shown in the image mosaic in Fig 1.

3. RESULTS

3.1. Photometry and spectral classification

³ <https://www2.keck.hawaii.edu/inst/lris/filters.html>

⁴ http://cfht.hawaii.edu/cgi-bin/elixir/skyprobe.pl?plot&mcal_20200323.png

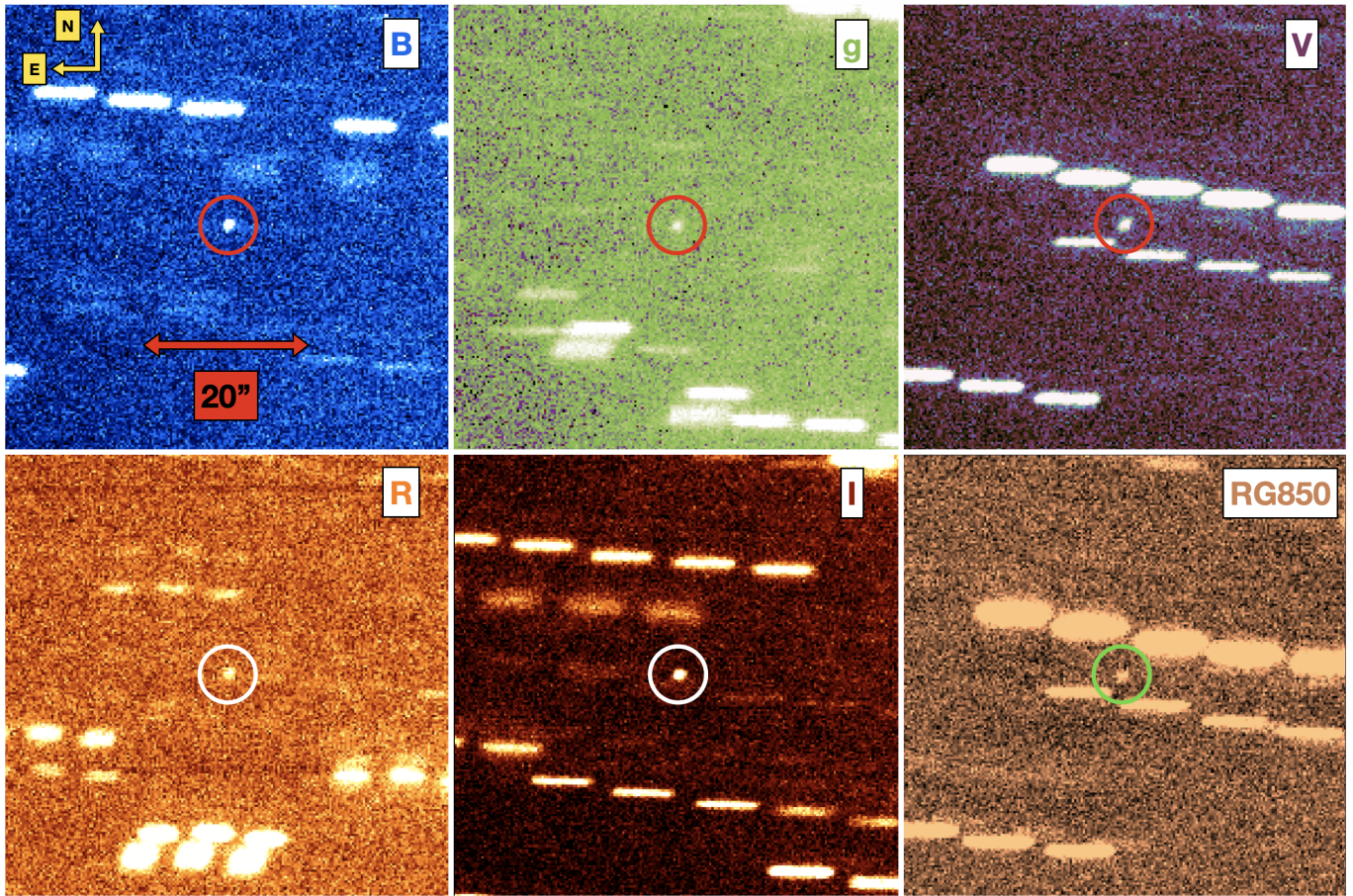


Figure 1. Top left panel: a 600 s equivalent exposure time robust mean stack of 5 x 120 s *B* filter images of 2020 CD₃. An arrow indicating the width of 20'' is shown for scale and the cardinal directions are indicated. Top center panel: a 600 s equivalent exposure time robust mean stack of 4 x 120 s *g* filter images of 2020 CD₃. Top right panel: a 600 s equivalent exposure time robust mean stack of 5 x 120 s *V* filter images of 2020 CD₃. Bottom left panel: a 180 s equivalent exposure time mean stack of 3 x 60 s *R* filter images of 2020 CD₃. Bottom center panel: a 960 s equivalent exposure time robust mean stack of 8 x 120 s *I* filter images of 2020 CD₃. Bottom right panel: a 600 s equivalent exposure time robust mean stack of 5 x 120 s RG850 filter images of 2020 CD₃.

We measured the photometry of 2020 CD₃ and the Solar analog stars using a 0.81'' aperture subtracting the median contribution from the sky background within a 2.5-3.5'' annulus. The *B*, *V*, *R* and *I* Johnson-Cousins and *g* SDSS filter photometry were calibrated using Solar analog stars from the Pan-STARRS catalog [Chambers et al. \(2016\)](#). The Pan-STARRS catalog magnitudes of the Solar analog stars were transformed to Johnson-Cousins and SDSS magnitudes using the conversions from [Tonry et al. \(2012\)](#). We obtain magnitudes $B = 25.11 \pm 0.05$, $g = 24.48 \pm 0.05$, $V = 24.21 \pm 0.05$, $R = 23.74 \pm 0.06$ and $I = 23.31 \pm 0.02$. In addition, we determine an RG850 magnitude of 23.88 ± 0.09 calibrated by using the equivalent SDSS *z* filter magnitudes determined for our Solar analog from the Pan-STARRS catalog. However, we caution the RG850 and SDSS *z* filters not being exactly alike, therefore our measured uncertainty is likely affected by small systematic differences between the RG850 and SDSS *z* filters and thus serves as a lower limit to its true RG850 magnitude.

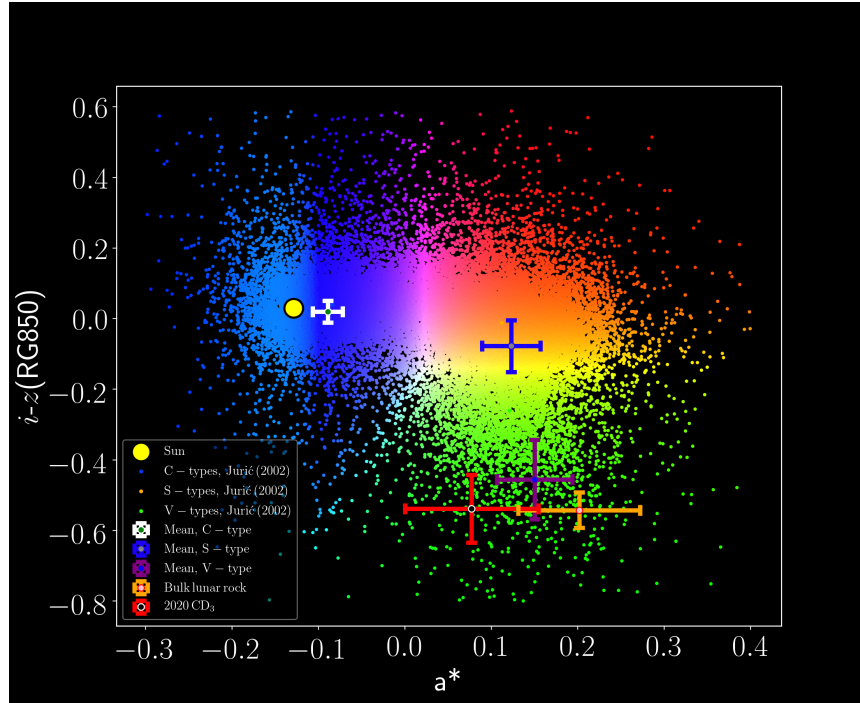


Figure 2. a^* vs. $i-z(\text{RG850})$ colors of 2020 CD₃ plotted with a^* vs. $i-z$ colors of C, S and V type asteroids (Ivezić et al. 2001; Jurić et al. 2002), active comets (Solontoi et al. 2012) and Kuiper Belt Objects (Ofek 2012). The colorization scheme of data points as a function of a^* and $i-z$ is adapted from Ivezić et al. (2002) where blue colors correspond to C-type asteroids, red colors correspond to S-type asteroids and green colors correspond to V-type asteroids. We note that in this case the measured RG850 magnitude of 2020 CD₃ is plotted as a substitute for its z magnitude.

The colors of 2020 CD₃ are $B-V = 0.90 \pm 0.07$, $V-g = -0.27 \pm 0.07$, $V-R = 0.46 \pm 0.08$, $R-I = 0.44 \pm 0.06$. The equivalent colors in SDSS bands are $g-r = 0.62 \pm 0.08$, $r-i = 0.21 \pm 0.06$ using the filter transformations from Jordi et al. (2006). In addition, we determine an $i\text{-RG850}$ color of -0.54 ± 0.10 . The $B-I$ color of 2020 CD₃ is 1.80 ± 0.05 corresponding to a reflective spectral slope between 434 nm and 761 nm of $18 \pm 3\%/100$ nm, indicating a surface significantly redder than the Sun ($B-I = 1.33$, Holmberg et al. 2006). In addition, the parameter $a^* = (0.89(g-r)) + (0.45(r-i)) - 0.57$, which is an indicator of reflective spectral slope (Ivezić et al. 2001), is equal to 0.08 ± 0.08 and is plotted vs. $i-z(\text{RG850})$ in Fig. 2. Compared to other asteroids, the $a^* = 0.08 \pm 0.08$ and $i-z(\text{RG850}) = -0.54 \pm 0.10$ has broad overlap with other V-type asteroids which have on average $a^* = 0.15 \pm 0.11$ and $i-z = -0.46 \pm 0.04$, (Jurić et al. 2002).

To compute the reflectivity spectrum of 2020 CD₃, we divide the flux per B , g , V , R , I and RG850 filter obtained for 2020 CD₃ by the flux of the Solar analog flux in each corresponding filter. We then normalize the reflectivity spectrum of to 550 nm and detrend the data using a fit of the spectrum with the function

$$r = 1 + a(\lambda - 550 \text{ nm}) \quad (1)$$

from Bus & Binzel (2002) where r is the normalized reflectivity as a function of λ and a is the spectral slope. The fit used to detrend the data from this function is made by fitting all B , g , V , R , I and RG850 data between 435 nm and 912 nm. The resulting normalized reflectivity spectrum is plotted in Fig. 3. The normalized reflectivity spectrum of 2020 CD₃ is most similar to the spectral range

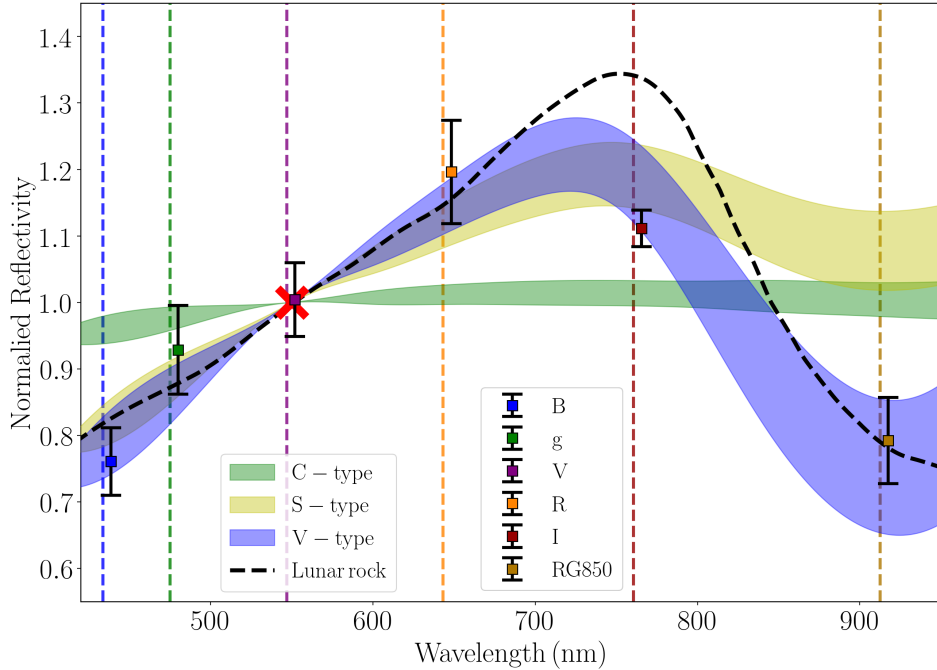


Figure 3. Reflectance photometric spectrum of 2020 CD₃ consisting of B , g , V , R , I and RG850 observations of 2020 CD₃ on 2020 March 23 UTC. The λ_{eff} locations of the B , g , V , R , I and RG850 filters have been plotted as vertical dashed lines. The data points for the normalized reflectivity of 2020 CD₃ have been offset slightly from their location in the wavelength direction. The error bars on the spectrum data points correspond to 1σ uncertainty. The spectrum has been normalized to unity at 550 nm indicated by the red cross. The spectral range of S, V and C-type asteroids from the Bus-DeMeo asteroid taxonomic catalog (DeMeo et al. 2009) are over-plotted with the V-type spectrum most closely resembling the spectra of 2020 CD₃. The average spectrum of coarse bulk Lunar rock samples is plotted for reference (Isaacson et al. 2011).

of V-type asteroids (Bus & Binzel 2002; DeMeo et al. 2009) with a red slope between 430 nm and 760 nm deep absorption feature in the vicinity of the RG850 data point at ~ 1000 nm compared to the reflectivity spectra of S and C-type asteroids (DeMeo et al. 2009). We note the same similarity in a^* vs. $i-z(\text{RG850})$ colors between 2020 CD₃ and V-type asteroids as seen in Fig. 2 as with our normalized reflectivity spectrum. This absorption feature at ~ 1000 nm as seen for basaltic V-type asteroids found through the inner Main Belt is due to the presence of large amounts of pyroxene minerals on the asteroid’s surface (Moskovitz et al. 2008). In addition, we note the same similarity between the spectrum of 2020 CD₃ and bulk basaltic Lunar rock consisting of pyroxenes minerals (Isaacson et al. 2011).

3.2. Lightcurve, periodicity and axial ratio estimation

In addition to measuring the photometry of 2020 CD₃ in the per filter B , g , V , R , I and RG850 composite image stacks, we search for lightcurve variations by measuring the photometry in our individual B , g , V and R filter observations. The measured photometric values in the individual images are presented in Table 1. We used the colors measured from our composite image stacks

described in Section 3.1 and photo-spectrum to convert our B , g and R measurements to their equivalent value in V . Using our V magnitudes and the following equation:

$$H = V - 5 \log_{10}(r_h \Delta) + 2.5 \log_{10} [(1 - G) \Phi_1(\alpha) + G \Phi_2(\alpha)] \quad (2)$$

from [Bowell et al. \(1988\)](#) where r_h is the 1.0059 au heliocentric distance of 2020 CD₃ on 2020 March 23 UTC, Δ is its geocentric distance of 0.0128 au and α is its phase angle of 45.4063°. G is the phase coefficient which we use the value of 0.25, the average value of G for S or Q-type asteroids ([Vereš et al. 2015](#)). $\Phi_1(\alpha)$ and $\Phi_2(\alpha)$ are the basis functions normalized at $\alpha = 0^\circ$ described in ([Bowell et al. 1988](#)). We detrend the values of H inferred from Eq. 2 dividing them by a linear fit which are plotted in the top panel of Fig. 4 which a median value of $H = 31.9 \pm 0.1$. The errors on these H measurements may be underestimated in part due to the unknown phase function of 2020 CD₃.

As seen in Fig. 4, there is brightness variability larger than the ~ 0.01 photometric scatter measured from the CFHT Skyprobe and the typical ~ 0.1 mag uncertainty of the data at SNR ~ 10 . Therefore, we will attempt to search for possible periodicities caused by time-variability in 2020 CD₃'s reflective cross-section over its rotation ([Barucci & Fulchignoni 1982](#)). We apply the Lomb-Scargle periodogram ([Lomb 1976](#)) to the detrended H magnitude data which is displayed in the top panel of Fig. 5. Removal of the linear trend over the ~ 1 h observing period will affect the determination of lightcurve periods that are on ~ 1 h time scales, but do not affect periodicities on ~ 100 s time scales. The highest peak in the lightcurve period vs. spectral power curve is located at ~ 573.4 s with a formal significance of $p \simeq 10^{-4}$. We apply bootstrap estimation ([Press et al. 1986](#)) of the uncertainties by removing \sqrt{N} data points from the time series lightcurve and repeating our periodogram estimation of the lightcurve period 10,000 times resulting in a central value of ~ 574.5 s and a 1σ uncertainty estimate of ~ 30.5 s. As an independent check of our results obtained with the Lomb-Scargle periodogram, we apply phase dispersion minimization analysis to our data ([Stellingwerf 1978](#)) and obtain a result of ~ 561.6 s compatible with the lightcurve period estimate obtained with the Lomb-Scargle periodogram as seen in the bottom panel of Fig. 5. For comparison, the meter-scale asteroids 2006 RH₁₂₀ and 2015 TC₂₅ both had lightcurve periods on the order of 60-120 s measured from photometry and radar observations. Furthermore, the ensemble of the available catalog of asteroid lightcurve periods available from the Asteroid Lightcurve Database ([Warner et al. 2009](#)) seems to indicate that asteroids smaller than 10 m can have rotation periods much shorter than 60 s ([Bolin et al. 2014](#)).

We can estimate a rough shape for 2020 CD₃ by assuming it possesses a triaxial prolate shape with dimensions, $a:b:c$ where $b \geq a \geq c$ in rough approximation with the shapes of other asteroids inferred from lightcurve inversion ([Harris et al. 2009](#); [Durech et al. 2010](#)). Assuming $a=c$, the ratio between b/a is described by $b/a = 10^{0.4A}$ where A is the peak-to-trough lightcurve amplitude ([Binzel et al. 1989](#)) resulting in a b/a of ~ 2.5 for 2020 CD₃ with lightcurve amplitude of ~ 1 mag. However, the combination of the significant phase angle of $\sim 45^\circ$ 2020 CD₃ was observed on 2020 March 23 UTC and the light scattering properties of its presumably rough surface may have had the effect of amplifying its observed lightcurve amplitude ([Zappala et al. 1990](#)). The relationship between the observed lightcurve amplitude at a given phase angle α and the lightcurve amplitude it would have if observed at $\alpha = 0^\circ$ is given by

$$\Delta m_{\alpha=0^\circ} = \frac{\Delta m(\alpha)}{1 + s\alpha} \quad (3)$$

from [Zappala et al. \(1990\)](#), where s is in units of mag deg⁻¹ for which we adopt the mean value of 0.012 mag deg⁻¹ from light scattering experiment and observations of asteroids ([Gutiérrez et al.](#)

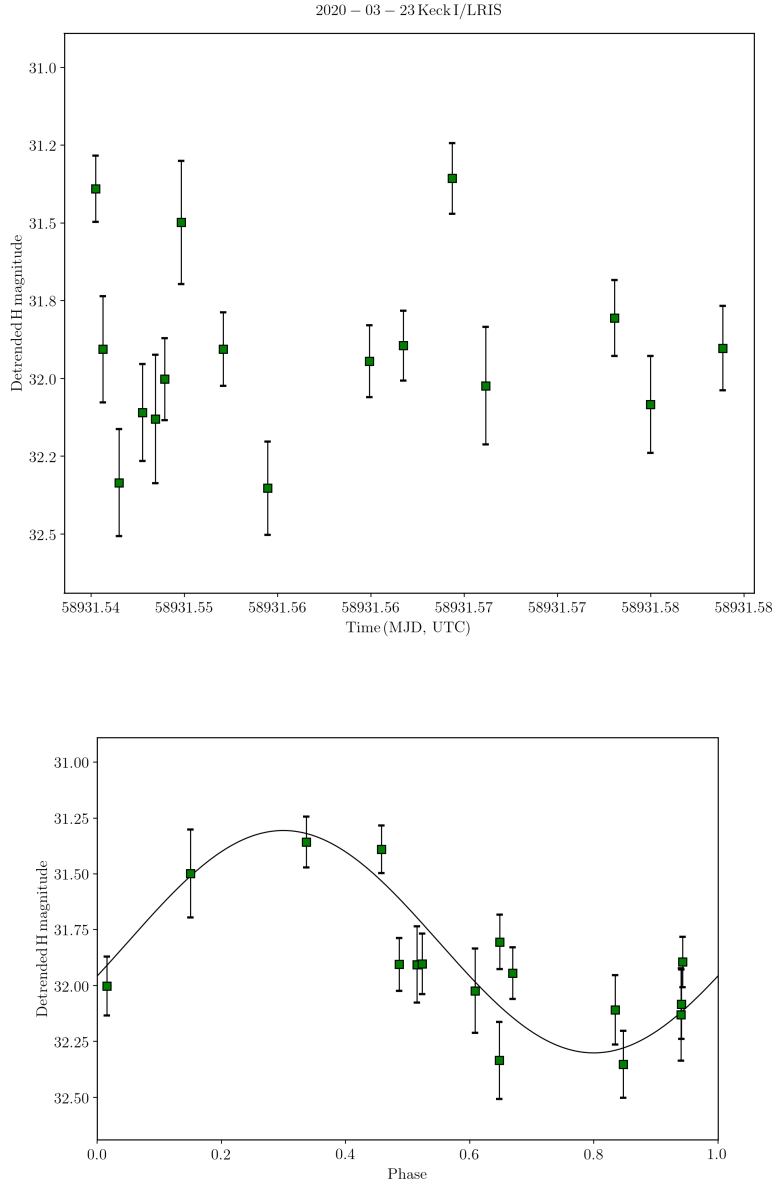


Figure 4. Top panel: Detrended H-magnitude lightcurve from 2020 March 23 UTC Keck I/LRIS B , g , V and R observations of 2020 CD₃ using a $0.81''$ radius aperture radii. The error bars on the data points are equal to their 1σ photometric uncertainties. The data have been detrended and points affected by trailed background stars have been removed. Bottom panel: phased 2020 March 23 UTC Keck I/LRIS observations corresponding to a single-peak lightcurve period of 573.4 s.

2006). Applying this correction to our observed lightcurve amplitude of ~ 1 magnitude lightcurve amplitude at $\sim 45^\circ$ phase angle, we calculate an equivalent $\alpha = 0^\circ$ lightcurve amplitude of ~ 0.6 mag.

In addition to the relationship between phase angle and lightcurve amplitude, the aspect angle of an asteroid when viewed from the Earth can also have an effect on its lightcurve amplitude (e.g., Hanuš et al. 2018; Bolin 2019). Because the pole orientation of 2020 CD₃ is unknown, it is not possible for us to constrain its aspect viewing angle. Therefore, we adopt the approach of Bolin et al. (2018c)

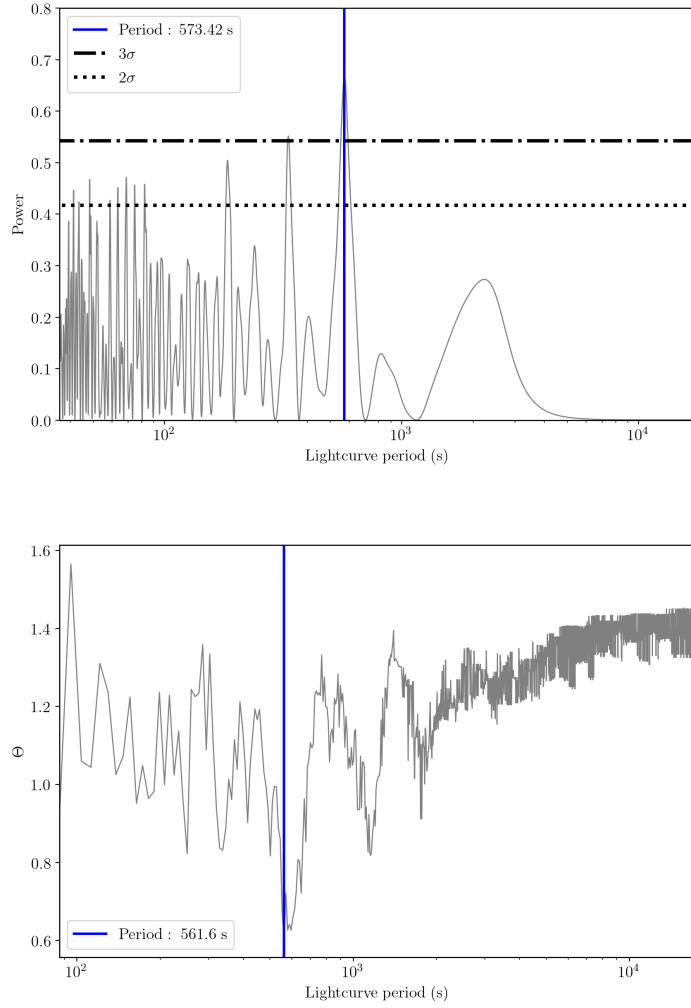


Figure 5. Top panel: Lomb-Scargle periodogram of lightcurve period vs. spectral power (Lomb 1976) for the Keck I/LRIS lightcurve data from the 2020 March 23 UTC observations. A peak in the power is located at double-peaked lightcurve period of 573.4 s. Bottom panel: Phase dispersion minimization analysis of lightcurve rotation period vs. Θ metric (Stellingwerf 1978). The Θ metric is minimized at double-peaked rotation periods of 561.6 s consistent with the 573.4 s rotation period found with the Lomb-Scargle Periodogram.

which is to average over all possible aspect angles using the following equation

$$\Delta m_{\text{diff}, \theta=90^\circ} = 1.25 \log \left(\frac{b^2 \cos^2 \theta + c^2 \sin^2 \theta}{a^2 \cos^2 \theta + c^2 \sin^2 \theta} \right) \quad (4)$$

from (Thirouin et al. 2016) which gives the lightcurve amplitude of an asteroid when viewed equatorially, i.e., at aspect angle, $\theta = 90^\circ$, and where a , b and c are the dimensions of 2020 CD₃. We will assume $1 \lesssim b/a \lesssim 2$ as observed in asteroid shape models inverted from lightcurves (Hanus et al. 2013; Durech et al. 2015) and $a = c$ for a prolate triaxial ellipsoid. Integrating Eq. 4 over all possible aspect angles results in $\Delta m_{\text{diff}} \simeq 0.5$. Therefore, we calculate the b/a ratio of 2020 CD₃ using $b/a = 10^{0.4A}$ where $A = (\Delta m_{\alpha=0^\circ} = 0.6$ from Eq. 3 + $\Delta m_{\text{diff}, \theta=90^\circ} = 0.5$ from Eq. 4) $\simeq 1$ corresponding to a b/a

~ 2.5 with the lightcurve amplitude phase angle and aspect angle effects roughly canceling each other out.

3.3. Astrometry, orbit determination and archival data search

In addition to measuring the photometry from our observations, we use the positions of 2020 CD₃ measured in our 3 x 30 s *R* filter images to refine the orbit of 2020 CD₃. We measured the astrometry of 2020 CD₃ with the Astrometrica software (Raab 2012) combined with reference stars from the *Gaia* data release 2 catalog (Gaia Collaboration et al. 2016, 2018). Table 2 contains our measured positions of 2020 CD₃ from our *R* filter observations. We conservatively estimate an astrometric uncertainty of 1.0'' in both the right ascension and declination directions to take into account the ~ 3 s timing uncertainty of the Keck I/LRIS instrument (Burdge et al. 2019) resulting in an increased $\sim 0.2''$ uncertainty in the along-track direction measured for the position of 2020 CD₃ in addition to our nominal astrometric uncertainty of $\sim 0.5''$. Adding to our 2020 March 23 UTC observations, we combine our observations with the publicly available observations of 2020 CD₃ measured by other observatories from the Minor Planet Center observation database⁵ In total, we use 60 observations of 2020 CD₃ taken between 2020 February 18 UTC and 2020 March 23 UTC in addition to our own observations that are listed in Table 2. Although uncertainty estimates for other observatories' measurements of asteroids exist (Vereš & Chesley 2017), we adopt conservative estimates for the astrometric uncertainties of $\sim 1.0''$ in both right ascension and declination for these other observatories' measured positions of 2020 CD₃. As an exception, we adopt the positional uncertainty of 0.4'' for the observations for 2020 CD₃ reported by T14, Mauna Kea, UH/Tholen NEO Follow-Up, made by the Canada France Hawaii Telescope and 0.8'' for observations made by J95, Great Shefford's 0.41 m telescope based on the historical astrometric performance made by these observatories described in the documentation for the orbit fitting software Find_Orb by Bill Gray⁶. We have submitted our astrometry of 2020 CD₃ on 2020 March 23 UTC to the Minor Planet Center which has appeared in MPEC 2020-O103⁷.

Using Find_Orb, we fit an orbit to our list of observations using the 8 planets and the Moon as perturbers. In addition to the six orbit parameters, semi-major axis, a , eccentricity, e , inclination, i , ascending node, Ω , argument of perihelion, ω , mean anomaly, M , we include an additional parameter to our orbital fit, the area-to-mass ratio (AMR) as a measure of the effect of Solar radiation pressure on the orbit of 2020 CD₃ (e.g., Micheli et al. 2012). The nominal orbital fit to our list of observations for the epoch of JD 2,458,931.5 (2020 March 23 UTC) in both heliocentric ($a, e, i, \Omega, \omega, M$) and geocentric orbital elements ($a_g, e_g, i_g, \Omega_g, \omega_g, M_g$), the AMR and H magnitude are given in Table 3. It can be noted that the Earth-similar heliocentric elements of $a \sim 1$ au, $e \sim 0.02$ and low inclination are typical properties of the minimoon population (Granvik et al. 2012; Fedorets et al. 2017).

The mean observed-minus-computed residual from our least squares orbital fit to the observations is 0.40'' with the Keck I/LRIS observations having observed-minus-computed residuals of $\sim 0.2''$ using the seven orbital parameter ($a, e, i, \Omega, \omega, M, \text{AMR}$ fit). By comparison, the six orbital parameter ($a, e, i, \Omega, \omega, M$) fit results in a slightly higher mean observed-minus-computed residual of 0.43''. The complete list of observed-minus-computed residuals for each of the 60 observations used to compute the orbit is given in Table 2. The e_g of 0.95821 at the epoch of our orbital fit corresponding

⁵ https://www.minorplanetcenter.net/tmp/2020_CD3.txt

⁶ https://www.projectpluto.com/find_orb.htm

⁷ <https://minorplanetcenter.net/mpec/K20/K200A3.html>

to the 2020 March 23 UTC data of our observations roughly indicates that 2020 CD₃'s orbit was approaching a $e_g > 1$ hyperbolic state for leaving the Earth-Moon system and the measured AMR of $6.96 \pm 2.41 \times 10^{-4}$ m²/kg is comparable to other small asteroids with measured AMRs (e.g., Micheli et al. 2013; Mommert et al. 2014; Farnocchia et al. 2017). In addition, 2020 CD₃'s i_g is retrograde with a value of 146.68615° and a geocentric perihelion, q_g , of 0.00031 au indicating that it is in the retrograde class of temporary natural satellites that come within the ~ 0.01 au Hill radius of the Earth (Urrutxua & Bombardelli 2017; Jedicke et al. 2018).

Our refined orbital solution of 2020 CD₃ from our 2020 March 23 UTC observations enabled the search for possible prediscoversy detections of 2020 CD₃ in the Zwicky Transient Facility (ZTF) archive (Masci et al. 2019) for additional refinement of the orbit (e.g., as for prediscoversy observations interstellar object 2I/Borisov by ZTF Bolin et al. 2020; Ye et al. 2020). The ZTF survey based on the Palomar Observatory's P48 Oschin Schmidt telescope consists of a number of survey programs, some that are open to the public and some that are internal to the ZTF collaboration and Caltech, that are designed to cover the entire sky and detect transient sources including Solar System asteroids and comets (Graham et al. 2019). The ZTF survey camera consists of a 576 megapixel array with a pixel scale of 1.01 arcseconds/pixel covering a 7.4-degree x 7.4-degree field of view (Dekany et al. 2016) and g , r and i band filters with a $r \sim 20.5$ to a SNR = 5 depth in a 30 s exposure generally used in survey (Bellm et al. 2019). The ZTF data system has the ability to detect both round, PSF-like detections (Masci et al. 2019) and fast-moving objects moving $> 5''/m$ resulting in the detections becoming significantly trailed (Ye et al. 2019a; Duev et al. 2019) in the survey's 30 s exposures. Therefore, because of its large field of view and ability to identify fast-moving objects, ZTF is the ideal system for ground-based detection of minimoons, objects that typically moving $> 10''/min$ or more (Bolin et al. 2014; Fedorets et al. 2020).

Extrapolating the trajectory of 2020 CD₃ as far back as 2018 October, we located regions of the sky where it was covered by the ZTF survey in g and r filters. We narrowed our search for prediscoversy observations to times when 2020 CD₃ was brighter than $V \sim 20$ taking into account the ~ 0.2 mag mean color differences between the standard Johnson V filter and the ZTF r filter for asteroids (Vereš & Chesley 2017). Our search revealed dates when 2020 CD₃ was brighter than $V \sim 20$ on 2019 January 17 UTC ($V \sim 19.1$), 2019 April 04 UTC ($V \sim 15.2$), 2019 November 15 UTC ($V \sim 19.5$) and 2020 February 13 UTC ($V \sim 17.0$). However, the only date overlapping with ZTF observations was on 2019 November 15 UTC in which a single g band exposure was obtained which was also during the full phase of the moon greatly increasing the sky background in the image. In addition, 2020 CD₃ was moving nearly $\sim 40''/min$ resulting in significant trailing losses (Shao et al. 2014) making its already difficult brightness of $V \sim 19.5$ impossible to detect. A possible method of detection for 2020 CD₃ is to use where its orbital trajectory overlaps with higher-cadence fields while it is moving with a slower rate of motion and use synthetic tracking to shift and stack along its possible trajectories increasing its detection's SNR to a detectable threshold as has been demonstrated for ZTF data of Main Belt and NEOs (Zhai et al. 2020), however, a full demonstration of synthetic tracking to locate 2020 CD₃ in ZTF data is beyond the scope of this work.

3.4. *Orbital evolution*

The second-known minimoon 2020 CD₃ was discovered while it was captured by the Earth-Moon system. To determine its orbital evolution before, during and after its captured state, we implemented the `rebound` n -body orbit integration package (Rein & Liu 2012) with our fitted orbit from Table 3.

In addition to its nominal orbit, we cloned ~ 10 additional massless test particles defined from the vertices of a cuboid represented by the heliocentric orbital elements and σ orbital parameter semi-major axis a , eccentricity e and inclination i uncertainties listed in Table. 3 and an initial ephemeris time of 2020 March 23 UTC. The simulations are run using the IAS15 integrator (Rein & Spiegel 2015) and the Sun, eight major masses of the Solar system, along with the Moon, Vesta, Ceres and Pluto⁸. The simulations were run using a timestep of 0.00249 y (21.825 hours, 0.03 times the Lunar orbital period), with an output of 0.01 y for 5-y and 100-y time-frames.

We adopt the definition of geocentric capture from Fedorets et al. (2017) and Jedicke et al. (2018) to describe the geocentric orbital evolution of 2020 CD₃, namely that while captured, 2020 CD₃ remains within 3 Hill radii (~ 0.03 au) of the Earth, has a $e_g < 1$, and approaches the Earth to within 1 Hill radius (~ 0.01 au) at some point during its captures. As seen in Fig. 6, 2020 CD₃, approaches the Earth-Moon system opposite from the Sun’s direction in the direction of the L2 Lagrange point with its capture beginning in mid 2018 with a low ~ 1 km/s encounter velocity. Almost half of minimoons pass through the L2 Lagrange point while becoming temporarily geocentrically bound (Granvik et al. 2012), therefore, it seems 2020 CD₃’s capture is non-exceptional in the case of temporarily captured asteroids. In addition, we see from the top panels of Fig. 6 that 2020 CD₃ is captured on a retrograde orbit $\sim 100^\circ$ and completes ~ 5 revolutions around the Earth-Moon system while remaining within three Hill radii of geocenter. Integrating its orbit forward and backward, the majority of 2020 CD₃ orbital clones remained captured within the Earth-Moon for ~ 2 y as seen in the bottom right panel of Fig.6 leaving the Earth-Moon system in mid 2020. Integrating the orbit with and without a Solar radiation pressure component does not significantly affect the capture duration of 2020 CD₃. The geocentric orbit of 2020 CD₃ is retrograde for nearly the entirety of its capture and its final orbit will result in it having a slightly larger heliocentric semi-major axis of a of 1.027 au compared to its pre-capture a of 0.973 au as seen in the bottom left panel of Fig. 6. Overall it seems the capture of 2020 CD₃ is a typical, however, having a longer duration than the ~ 1 y capture duration of 2006 RH₁₂₀, the only other known minimoon, and the ~ 9 month capture duration averaged over the minimoon population (Granvik et al. 2012).

In addition, we take a look at the longer term, 100 y heliocentric orbital evolution of 2020 CD₃ as presented in Figs. 7 and 8. Integrating the orbit of 2020 CD₃ 100 y into the past and into the future show similar behavior in that 2020 CD₃ has close encounters with the Earth placing 2020 CD₃ inside the Hill radius of the Earth every ~ 20 -30 y as seen in the bottom right panels of Figs. 7 and 8. The long-term orbit of 2020 CD₃ resembles a horseshoe orbit as seen in the upper left panels of Figs. 7 and 8 where its status as temporarily capture asteroids has resulted from its similar orbital plane and low encounter velocity relative to Earth’s (Granvik 2013; Jedicke et al. 2018). Interestingly, some of the 2020 CD₃ orbit clones when integrated into the future switch from a max inclination of 0.012° to 0.031° during the next encounter with the Earth. In addition, we have undertaken preliminary, long term simulations using the hybrid MERCURIUS rebound integrator, (Rein et al. 2019) using the same initial conditions as above, including the eight clones. These initial simulations indicate that the horse-shoe dynamical situation is stable for at least $\sim 10^6$ years.

4. DISCUSSION AND CONCLUSIONS

⁸ Taken from the JPL HORIZONS Solar System Dynamics Database <https://ssd.jpl.nasa.gov/> (Giorgini et al. 1996), on 10th April, 2020.

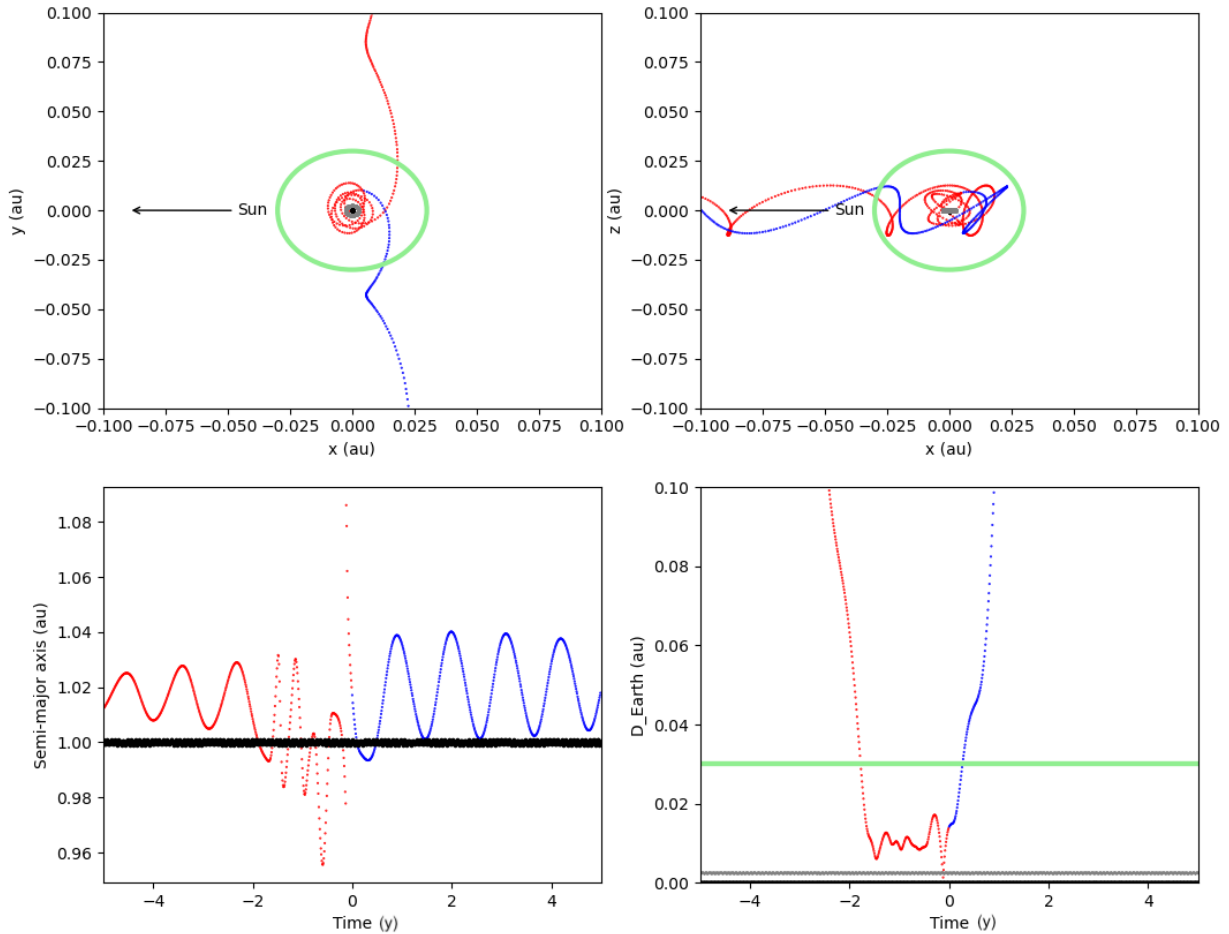


Figure 6. Top left panel: mean geocentric, co-rotating Cartesian y and x coordinates of 2020 CD₃ orbital clones ± 5 y centered on 2020 March 23 UTC encompassing its ~ 700 day capture completing ~ 5 revolutions around the Earth-Moon system. The red dotted line indicates the trajectory of 2020 CD₃ before 2020 March 23 UTC and the blue dotted line indicates the trajectory of 2020 CD₃ after 2020 March 23 UTC. A green circle with a radius of three times the Earth’s Hill radii of ~ 0.03 au is overlotted. The direction towards the Sun in the co-rotating frame is indicated. Top right panel: same as the top left panel except for mean geocentric, co-rotating Cartesian x and z coordinates. Bottom left panel: the evolution of 2020 CD₃’s orbital clones’ mean semi-major axes ± 5 y centered on 2020 March 23 UTC. The color code of the dotted lines is the same as in the top panels. Bottom right panel: the mean geocentric distance of 2020 CD₃ orbital clones ± 5 y centered on 2020 March 23 UTC. A horizontal green line indicates three times the Hill radii in distance. The color code of the dotted lines is the same as in the previous three panels.

It appears that 2020 CD₃ represents a typical case when compared to the known ensemble and dynamical path of minimoons. While it is difficult to estimate the true population of minimoons given the vast incompleteness of asteroid surveys (Jedicke et al. 2016) the discovery of 2020 CD₃ along with 2006 RH₁₂₀ confirm minimoons as viable members of the near-Earth object population

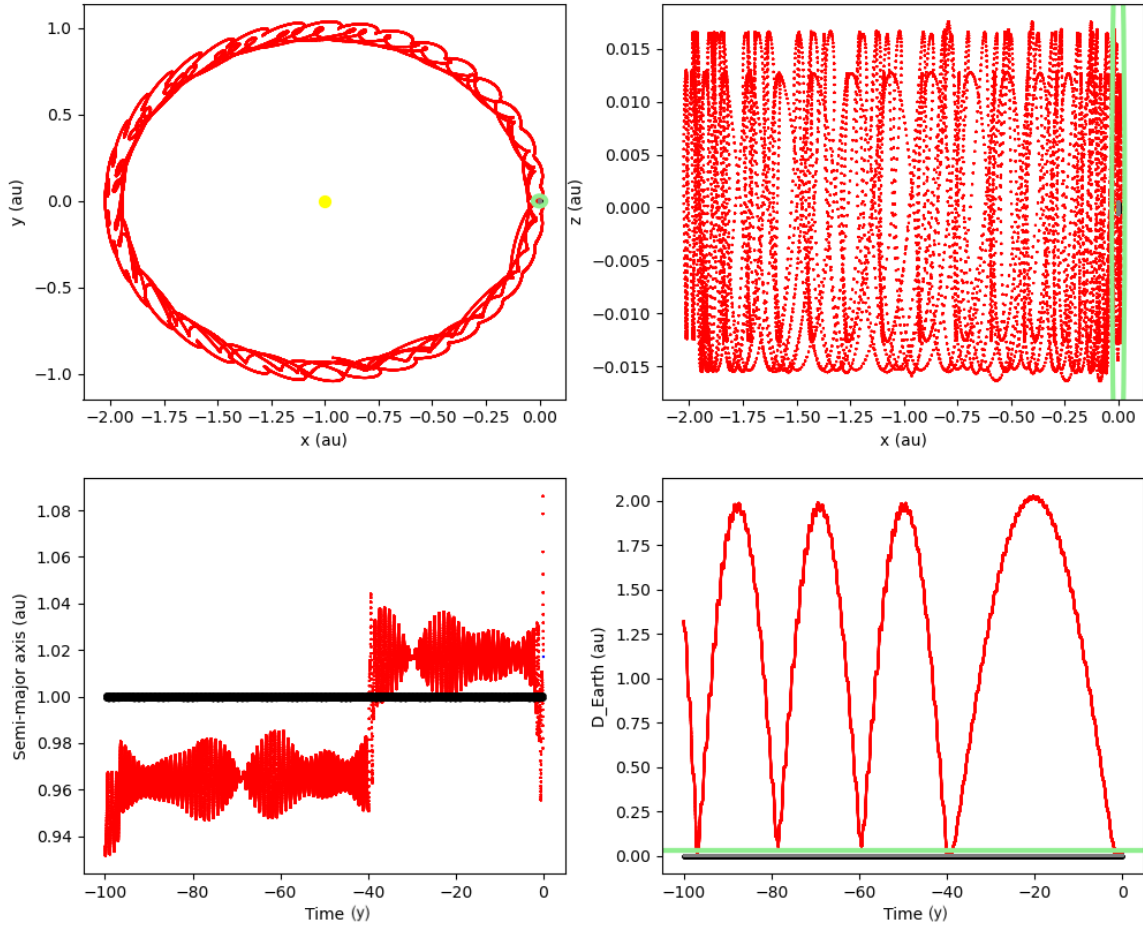


Figure 7. Top left panel: mean geocentric Cartesian y and x coordinates of 2020 CD₃ orbital clones integrated backwards 100 y from 2020 March 23 UTC (blue line) with the Earth’s three Hill radii marked in green. Top right panel: same as the top left panel except for the mean geocentric Cartesian x and z coordinates of 2020 CD₃ orbital clones integrated backwards 100 y from 2020 March 23 UTC. Bottom left panel: the evolution in 2020 CD₃’s orbital clones’ mean semi-major axis integrated backwards 100 y from 2020 March 23 UTC with the Earth’s orbit in black. Bottom right panel: the geocentric distance of 2020 CD₃ orbital clones integrated backwards 100 y from 2020 March 23 UTC.

and is the first minimoon to be spectrophotometrically characterized. It seems as its orbital dynamics are similar to co-orbitals of Earth (Morais & Morbidelli 2002) of which there is one known example, 2010 TK₇ (Connors et al. 2011) and quasi-satellites of which several are known, e.g., (469219) 2016 HO₃ (Chodas 2016). Compared to the asteroid population at large, out of ~ 1 million known asteroids as of 2020 July, only ~ 10 are of similar size as 2020 CD₃ with $H \sim 31$ or smaller making 2020 CD₃ one of the smallest asteroids discovered and characterizes with spectrophotometry (e.g., Reddy et al. 2016).

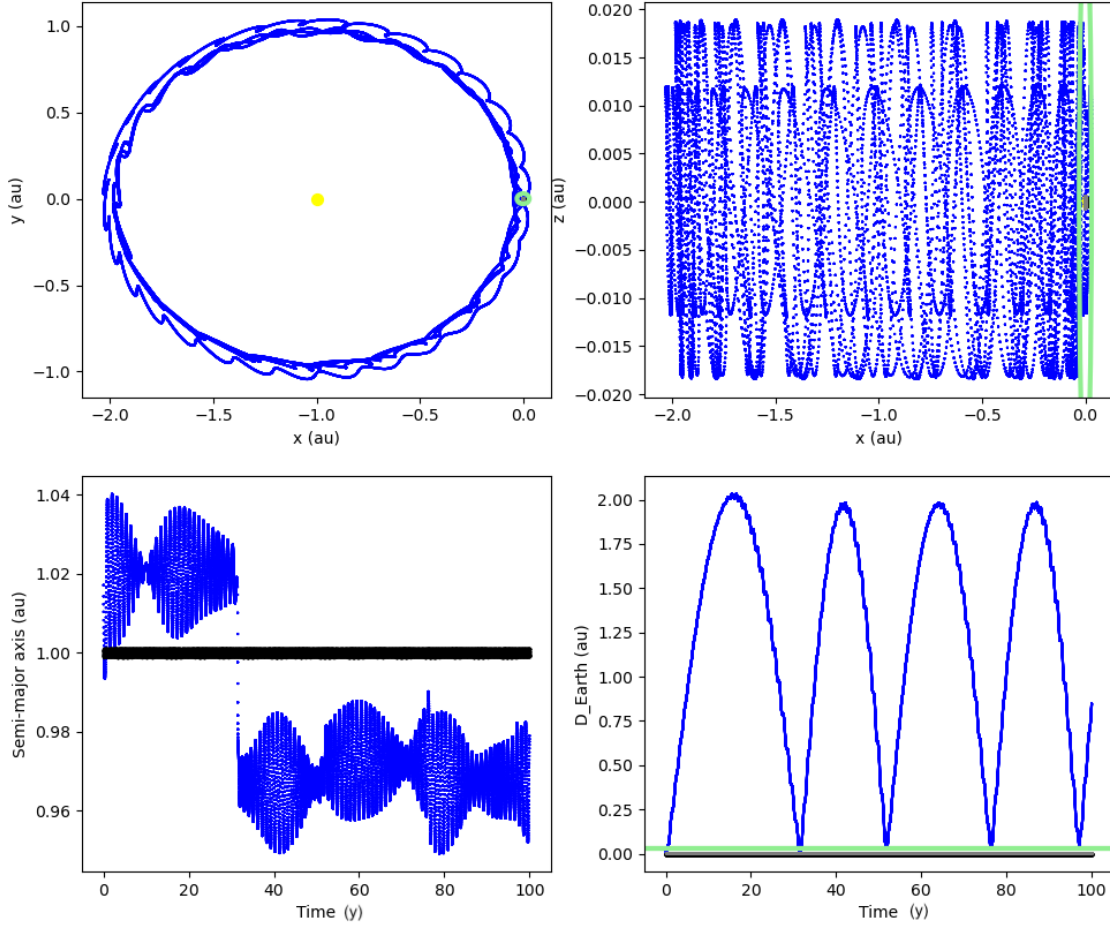


Figure 8. Top left panel: same as in Fig. 7 except for orbital clones of 2020 CD₃ integrated forwards 100 y from 2020 March 23 UTC (red line) with the Earth’s three Hill radii marked in green. Top right panel: same as the top left panel except for the mean geocentric Cartesian x and z coordinates of 2020 CD₃ orbital clones integrated forwards 100 y from 2020 March 23 UTC. Bottom left panel: the evolution in 2020 CD₃’s orbital clones’ mean semi-major axis integrated forwards 100 y from 2020 March 23 UTC with the Earth’s orbit in black. Bottom right panel: the geocentric distance of 2020 CD₃ orbital clones integrated forwards 100 y from 2020 March 23 UTC.

While its spectrum and colors seem to indicate that 2020 CD₃ is a likely V-type asteroid with an origin from the inner-Main Belt (DeMeo & Carry 2013) as discussed in Section 3.1, we can use its orbit in reference with models describing the NEO population (Granvik et al. 2016, 2018) as an independent indication of its source through asteroid escape pathways in the Main Belt (Granvik et al. 2017). Comparison with the NEO population model suggests that its most likely Main Belt escape source with $\sim 70\%$ probability was through the ν_6 resonance located near the inner edge of the Main Belt at 2.1 au for low inclination objects (Milani & Knežević 1990). The second and third most

likely sources are the Hungaria asteroid population located between 1.8 au and 2.0 au (Milani et al. 2010) with a $\sim 25\%$ probability and the 3:1 mean motion resonance located at the border between the inner and center Main Belt at 2.5 au (Wisdom 1983) with a $\sim 5\%$ probability. We note that the current NEO model is only available for asteroids with $H \leq 25$ or brighter, therefore we have made the comparison between 2020 CD₃ and the NEO model with the assumption that it has $H = 25$. Its other orbital parameters remain the same for the purposes of comparison with the NEO model.

Weighing the NEO albedo model (Morbidelli et al. 2020) according to these source probabilities for 2020 CD₃ results in a predicted albedo, p_v , of ~ 0.23 which is on the lower 0.25-0.45 p_v range of V-type asteroids (DeMeo & Carry 2013). Using our measured H magnitude of 31.9 ± 0.1 and the following equation relating the diameter D and p_v :

$$D = \frac{1329}{\sqrt{p_v}} 10^{-\frac{H}{5}} \quad (5)$$

from Harris & Lagerros (2002), we calculate that 2020 CD₃ has $D = 1.2 \pm 0.1$ m assuming $p_v = 0.23$ as determined for 2020 CD₃ from its possible Main Belt sources in the NEO albedo model (Morbidelli et al. 2020) or $D = 0.9 \pm 0.1$ m if using $p_v = 0.35$, the mean albedo of V-type asteroids in the Main Belt (DeMeo & Carry 2013) making it currently the smallest asteroid studied spectrophotometrically with the next smallest being asteroid 2015 TC₂₅ (Reddy et al. 2016).

We estimate the density of 2020 CD₃ by combining our constraints on its diameter and albedo combined with our AMR measurement from fitting its orbit. Using our measured AMR of $6.9 \pm 2.4 \times 10^{-4}$ m²/kg and diameter estimate of $D = 1.0 \pm 0.1$ m, we estimate the bulk density of 2020 CD₃ to be 2.1 ± 0.7 g/cm³ broadly compatible with the densities of other small asteroids determined from AMR measurements (e.g., Micheli et al. 2012). In comparison, the density of 2015 TC₂₅ is ~ 1 g/cm³ assuming a diameter of ~ 2.2 m (Reddy et al. 2016) and an AMR of $6-7 \times 10^{-4}$ m²/kg (Farnocchia et al. 2017). Assuming 0% macroporosity, the total mass of 2020 CD₃ is $\sim 10^4$ kg.

While its estimated density of 2.1 ± 0.7 g/cm³ is broadly consistent with the density of V-type asteroids which have bulk densities of ~ 2.3 g/cm³ (Carry 2012) which its spectrum resembles, it is likely, however, that 2020 CD₃ has a porosity in the range of $\sim 10\%$ - 20% as for meteorites (Consolmagno et al. 2008), its closest analog as one of the smallest known asteroids. In contrast, the km-scale V-type asteroids which we are drawing in comparison with 2020 CD₃ have macroporosities of $\sim 30\%$ or larger (Carry 2012) resulting in a higher density when correcting their ~ 2.3 g/cm³ bulk densities for their higher macroporosity. Therefore, it may be more appropriate to compare the density of 2020 CD₃ with achondritic basaltic meteorites which typically have bulk densities of ~ 3.0 g/cm³ which is somewhat larger than our estimated range of the density of 2020 CD₃.

2020 CD₃ is likely the product of the fragmentation of a larger parent asteroid given its small ~ 1 m size and its correspondingly short < 1 Myr time scale (Bottke et al. 2005). There appears to be some discrepancy in the fact that 2020 CD₃ most likely originates in the 1.8-2.2 au range at the inner edge of the Main Belt while having a spectrum similar to V-type asteroids which are thought to originate from the asteroid (4) Vesta (Binzel & Xu 1993; Parker et al. 2008) and are primarily located at ~ 2.3 au (DeMeo & Carry 2013). A significant number of V-type asteroids exist further from the Sun located past 2.5 au in the central Main Belt (Carruba et al. 2005; Migliorini et al. 2017) which could provide a possible source of Earth-crossing V-type NEOs like 2020 CD₃ if they were to drift inward into the 3:1 resonance due to the thermal recoil Yarkovsky effect (Farinella et al. 1998).

However, the role of the 3:1 resonance in transporting 2020 CD₃ into Earth-crossing space from the Main Belt seems unlikely due to its $\sim 5\%$ source probability. In addition, the Yarkovsky effect is able to transport meter-scale objects like 2020 CD₃ into the proximity of the ν_6 resonance, the most likely source of 2020 CD₃, in < 1 Myrs if it were to have originated as a fragment at 2.3 au (Bottke et al. 2006; Vokrouhlický et al. 2015) where most V-type asteroids are found even if possesses significantly different thermal inertia properties compared to larger, km-scale asteroids (Delbo et al. 2007; Bolin et al. 2018a). In addition, is apparent from the wide distribution of $\lesssim 1$ km Vesta family fragments covering the entirety of the inner Main Belt (Bolin et al. 2017) that the size-dependent velocity distribution of family fragments originating from Vesta could have placed 2020 CD₃-sized objects anywhere between the nu_6 resonance at ~ 2.2 au and the 3:1 resonance at 3.5 au (Carruba & Nesvorný 2016; Bolin et al. 2018b). Therefore, the location of the ν_6 resonance at the inner edge of the Main Belt at 2.2 au as the most likely source of 2020 CD₃ does not necessarily preclude asteroids far from its vicinity as the original parent body of 2020 CD₃.

Besides collisions, rotational fission of asteroids that are spinning near their rotational stability limit could be a possible origin of 2020 CD₃ (Walsh et al. 2008). Several asteroids have been observed to be in the act of rotationally shedding mass or fragmenting (e.g., Moreno et al. 2017; Jewitt et al. 2017; Ye et al. 2019b) or have a dynamically-associated cluster of asteroids compatible with a fragmentation event in the recent past due to their rotation (Vokrouhlický et al. 2017). In addition, binary asteroids systems can become decoupled over time due to the influence of thermal radiation recoil effects (McMahon & Scheeres 2010) which can result in small asteroids like 2020 CD₃ leaving their binary systems and entering Earth-crossing space. The fragmentation of asteroid parent bodies or decoupling of binary systems can occur while an asteroid parent body in near-Earth object space (Scheirich et al. 2019; Bottke et al. 2020) providing an origin for 2020 CD₃ outside of the Main Belt.

Another possible origin of minimoons is from Lunar impacts. While the orbits of Lunar debris dynamically decay after a few kyrs, it is possible that some Lunar ejecta can be re-captured by the Earth-Moon system as minimoons due to their orbital similarity with the Earth (Gladman et al. 1995). As presented in Fig. 3, the spectrum of 2020 CD₃ is compatible with the spectrum of bulk Lunar rock at the precision of our spectrophotometry. In addition, our inferred density of 2020 CD₃ of 2.1 ± 0.7 g/cm³ is similar impact basin ejecta Lunar rock which have bulk density (~ 2.4 g/cm³ Kiefer et al. 2012) and $\sim 20\%$ porosity. Under the assumption that 2020 CD₃ originated as Lunar ejecta, the young, $\lesssim 1$ Myr-scale cosmic-ray exposure ages of Lunar meteorites (Eugster et al. 2006) implies that the vast majority of Lunar meteorites and 2020 CD₃ by extension had to have been produced by a large and recent Lunar impact. The most recent, large impact that could produce ejecta the size of 2020 CD₃ is the Giordano Bruno crater that has been estimated to be ~ 4 Myrs old (Morota et al. 2009) based on the occurrence of craters near its proximity. However, the Lunar ejecta origin of 2020 CD₃ is diminished by the fact that the vast majority Lunar meteorites possess cosmic ray exposure ages much shorter than the 4 Myr age of the Giordano Bruno crater suggesting that the dominant source of recent Lunar meteorites and thus Lunar ejecta are much smaller, more recent impact events than could have produced ejecta the size of 2020 CD₃ (Minton et al. 2019).

This work was supported by the GROWTH project funded by the National Science Foundation under PIRE Grant No 1545949.

Some of the data presented herein were obtained at the W. M. Keck Observatory, which is operated as a scientific partnership among the California Institute of Technology, the University of California and the National Aeronautics and Space Administration. The Observatory was made possible by the generous financial support of the W. M. Keck Foundation.

The authors wish to recognize and acknowledge the very significant cultural role and reverence that the summit of Maunakea has always had within the indigenous Hawaiian community. We are most fortunate to have the opportunity to conduct observations from this mountain.

C.F. gratefully acknowledges the support of his research by the Heising-Simons Foundation (#2018-0907).

M. W. Coughlin acknowledges support from the National Science Foundation with grant number PHY-2010970.

Based on observations obtained with the Samuel Oschin Telescope 48-inch and the 60-inch Telescope at the Palomar Observatory as part of the Zwicky Transient Facility project. ZTF is supported by the National Science Foundation under Grant No. AST-1440341 and a collaboration including Caltech, IPAC, the Weizmann Institute for Science, the Oskar Klein Center at Stockholm University, the University of Maryland, the University of Washington, Deutsches Elektronen-Synchrotron and Humboldt University, Los Alamos National Laboratories, the TANGO Consortium of Taiwan, the University of Wisconsin at Milwaukee, and Lawrence Berkeley National Laboratories. Operations are conducted by COO, IPAC, and UW.

This work has made use of data from the European Space Agency (ESA) mission *Gaia* (<https://www.cosmos.esa.int/gaia>), processed by the *Gaia* Data Processing and Analysis Consortium (DPAC, <https://www.cosmos.esa.int/web/gaia/dpac/consortium>). Funding for the DPAC has been provided by national institutions, in particular the institutions participating in the *Gaia* Multilateral Agreement.

Facility: Keck I Telescope, P48 Oschin Schmidt telescope/Zwicky Transient Facility

REFERENCES

- Barucci, M. A., & Fulchignoni, M. 1982, *Moon and Planets*, 27, 47
- Bellm, E. C., Kulkarni, S. R., Graham, M. J., et al. 2019, 131, 018002, doi: [10.1088/1538-3873/aaecbe](https://doi.org/10.1088/1538-3873/aaecbe)
- Binzel, R. P., Farinella, P., Zappalà, V., & Cellino, A. 1989, in *Asteroids II*, ed. R. P. Binzel, T. Gehrels, & M. S. Matthews, 416–441
- Binzel, R. P., & Xu, S. 1993, *Science*, 260, 186, doi: [10.1126/science.260.5105.186](https://doi.org/10.1126/science.260.5105.186)
- Bolin, B., Jedicke, R., Granvik, M., et al. 2014, *Icarus*, 241, 280, doi: [10.1016/j.icarus.2014.05.026](https://doi.org/10.1016/j.icarus.2014.05.026)
- Bolin, B. T. 2019, arXiv e-prints, arXiv:1912.07386, <https://arxiv.org/abs/1912.07386>
- Bolin, B. T., Delbo, M., Morbidelli, A., & Walsh, K. J. 2017, *Icarus*, 282, 290, doi: [10.1016/j.icarus.2016.09.029](https://doi.org/10.1016/j.icarus.2016.09.029)
- Bolin, B. T., Morbidelli, A., & Walsh, K. J. 2018a, *A&A*, 611, A82, doi: [10.1051/0004-6361/201732079](https://doi.org/10.1051/0004-6361/201732079)
- Bolin, B. T., Walsh, K. J., Morbidelli, A., & Delbo, M. 2018b, *MNRAS*, 473, 3949, doi: [10.1093/mnras/stx2546](https://doi.org/10.1093/mnras/stx2546)
- Bolin, B. T., Weaver, H. A., Fernandez, Y. R., et al. 2018c, *ApJL*, 852, L2, doi: [10.3847/2041-8213/aaa0c9](https://doi.org/10.3847/2041-8213/aaa0c9)
- Bolin, B. T., Lisse, C. M., Kasliwal, M. M., et al. 2020, *AJ*, 160, 26, doi: [10.3847/1538-3881/ab9305](https://doi.org/10.3847/1538-3881/ab9305)

- Bottke, W. F., Durda, D. D., Nesvorný, D., et al. 2005, *Icarus*, 179, 63, doi: [10.1016/j.icarus.2005.05.017](https://doi.org/10.1016/j.icarus.2005.05.017)
- Bottke, W. F., Moorhead, A., Hergenrother, C. W., et al. 2020, in *Lunar and Planetary Science Conference, Lunar and Planetary Science Conference*, 1215
- Bottke, Jr., W. F., Vokrouhlický, D., Rubincam, D. P., & Nesvorný, D. 2006, *Annual Review of Earth and Planetary Sciences*, 34, 157, doi: [10.1146/annurev.earth.34.031405.125154](https://doi.org/10.1146/annurev.earth.34.031405.125154)
- Bowell, E., Hapke, B., Domingue, D., et al. 1988, *Asteroids II*, 399
- Burdge, K. B., Fuller, J., Phinney, E. S., et al. 2019, *ApJL*, 886, L12, doi: [10.3847/2041-8213/ab53e5](https://doi.org/10.3847/2041-8213/ab53e5)
- Bus, S. J., & Binzel, R. P. 2002, *Icarus*, 158, 146, doi: [10.1006/icar.2002.6856](https://doi.org/10.1006/icar.2002.6856)
- Carruba, V., Michtchenko, T. A., Roig, F., Ferraz-Mello, S., & Nesvorný, D. 2005, *A&A*, 441, 819, doi: [10.1051/0004-6361:20053355](https://doi.org/10.1051/0004-6361:20053355)
- Carruba, V., & Nesvorný, D. 2016, *MNRAS*, 457, 1332, doi: [10.1093/mnras/stw043](https://doi.org/10.1093/mnras/stw043)
- Carry, B. 2012, *Planet. Space Sci.*, 73, 98, doi: [10.1016/j.pss.2012.03.009](https://doi.org/10.1016/j.pss.2012.03.009)
- Chambers, K. C., Magnier, E. A., Metcalfe, N., et al. 2016, *ArXiv e-prints*. <https://arxiv.org/abs/1612.05560>
- Chodas, P. 2016, in *AAS/Division for Planetary Sciences Meeting Abstracts #48, AAS/Division for Planetary Sciences Meeting Abstracts*, 311.04
- Chyba, M., Patterson, G., Picot, G., et al. 2014, *Journal of Industrial and Management Optimization*, 10, 477
- Connors, M., Wiegert, P., & Veillet, C. 2011, *Nature*, 475, 481, doi: [10.1038/nature10233](https://doi.org/10.1038/nature10233)
- Consolmagno, G., Britt, D., & Macke, R. 2008, *Chemie der Erde / Geochemistry*, 68, 1, doi: [10.1016/j.chemer.2008.01.003](https://doi.org/10.1016/j.chemer.2008.01.003)
- de la Fuente Marcos, C., & de la Fuente Marcos, R. 2016, *MNRAS*, 462, 3441, doi: [10.1093/mnras/stw1972](https://doi.org/10.1093/mnras/stw1972)
- Dekany, R., Smith, R. M., Belicki, J., et al. 2016, in *Society of Photo-Optical Instrumentation Engineers (SPIE) Conference Series, Vol. 9908, Proc. SPIE*, 99085M
- Delbo, M., dell'Oro, A., Harris, A. W., Mottola, S., & Mueller, M. 2007, *Icarus*, 190, 236, doi: [10.1016/j.icarus.2007.03.007](https://doi.org/10.1016/j.icarus.2007.03.007)
- DeMeo, F. E., Binzel, R. P., Slivan, S. M., & Bus, S. J. 2009, *Icarus*, 202, 160, doi: [10.1016/j.icarus.2009.02.005](https://doi.org/10.1016/j.icarus.2009.02.005)
- DeMeo, F. E., & Carry, B. 2013, *Icarus*, 226, 723, doi: [10.1016/j.icarus.2013.06.027](https://doi.org/10.1016/j.icarus.2013.06.027)
- Duev, D. A., Mahabal, A., Ye, Q., et al. 2019, *MNRAS*, 486, 4158, doi: [10.1093/mnras/stz1096](https://doi.org/10.1093/mnras/stz1096)
- Durech, J., Carry, B., Delbo, M., Kaasalainen, M., & Viikinkoski, M. 2015, *Asteroid Models from Multiple Data Sources*, 183–202
- Durech, J., Sidorin, V., & Kaasalainen, M. 2010, *A&A*, 513, A46, doi: [10.1051/0004-6361/200912693](https://doi.org/10.1051/0004-6361/200912693)
- Elvis, M., McDowell, J., Hoffman, J. A., & Binzel, R. P. 2011, *Planet. Space Sci.*, 59, 1408, doi: [10.1016/j.pss.2011.05.006](https://doi.org/10.1016/j.pss.2011.05.006)
- Eugster, O., Herzog, G. F., Marti, K., & Caffee, M. W. 2006, *Irradiation Records, Cosmic-Ray Exposure Ages, and Transfer Times of Meteorites*, ed. D. S. Lauretta & H. Y. McSween, 829
- Farinella, P., Vokrouhlický, D., & Hartmann, W. K. 1998, *Icarus*, 132, 378
- Farnocchia, D., Tholen, D. J., Micheli, M., et al. 2017, in *AAS/Division for Planetary Sciences Meeting Abstracts #49, AAS/Division for Planetary Sciences Meeting Abstracts*, 100.09
- Fedorets, G., Granvik, M., & Jedicke, R. 2017, *Icarus*, 285, 83, doi: [10.1016/j.icarus.2016.12.022](https://doi.org/10.1016/j.icarus.2016.12.022)
- Fedorets, G., Granvik, M., Jones, R. L., Jurić, M., & Jedicke, R. 2020, *Icarus*, 338, 113517, doi: [10.1016/j.icarus.2019.113517](https://doi.org/10.1016/j.icarus.2019.113517)
- Flewelling, H. A., Magnier, E. A., Chambers, K. C., et al. 2016, *ArXiv e-prints*. <https://arxiv.org/abs/1612.05243>
- Fukugita, M., Ichikawa, T., Gunn, J. E., et al. 1996, *AJ*, 111, 1748, doi: [10.1086/117915](https://doi.org/10.1086/117915)
- Gaia Collaboration, Prusti, T., de Bruijne, J. H. J., et al. 2016, *A&A*, 595, A1, doi: [10.1051/0004-6361/201629272](https://doi.org/10.1051/0004-6361/201629272)
- Gaia Collaboration, Brown, A. G. A., Vallenari, A., et al. 2018, *A&A*, 616, A1, doi: [10.1051/0004-6361/201833051](https://doi.org/10.1051/0004-6361/201833051)
- Giorgini, J. D., Yeomans, D., Chamberlin, A., et al. 1996, in *Bulletin of the American Astronomical Society, Vol. 28, AAS/Division for Planetary Sciences Meeting Abstracts #28*, 1158

- Gladman, B. J., Burns, J. A., Duncan, M. J., & Levison, H. F. 1995, *Icarus*, 118, 302, doi: [10.1006/icar.1995.1193](https://doi.org/10.1006/icar.1995.1193)
- Graham, M. J., Kulkarni, S. R., Bellm, E. C., et al. 2019, *PASP*, 131, 078001, doi: [10.1088/1538-3873/ab006c](https://doi.org/10.1088/1538-3873/ab006c)
- Granvik, M., Morbidelli, A., Vokrouhlický, D., et al. 2017, *A&A*, 598, A52, doi: [10.1051/0004-6361/201629252](https://doi.org/10.1051/0004-6361/201629252)
- Granvik, M., Vaubaillon, J., & Jedicke, R. 2012, *Icarus*, 218, 262, doi: [10.1016/j.icarus.2011.12.003](https://doi.org/10.1016/j.icarus.2011.12.003)
- Granvik, M., Morbidelli, A., Jedicke, R., et al. 2016, *Nature*, 530, 303, doi: [10.1038/nature16934](https://doi.org/10.1038/nature16934)
- . 2018, *Icarus*, 312, 181, doi: [10.1016/j.icarus.2018.04.018](https://doi.org/10.1016/j.icarus.2018.04.018)
- Granvik, M.; Jedicke, R. 2013 (XXX), XXX
- Gutiérrez, P. J., Davidsson, B. J. R., Ortiz, J. L., Rodrigo, R., & Vidal-Núñez, M. J. 2006, *A&A*, 454, 367, doi: [10.1051/0004-6361:20064838](https://doi.org/10.1051/0004-6361:20064838)
- Hanuš, J., Ďurech, J., Brož, M., et al. 2013, *A&A*, 551, A67, doi: [10.1051/0004-6361/201220701](https://doi.org/10.1051/0004-6361/201220701)
- Hanuš, J., Delbo, M., Alí-Lagoa, V., et al. 2018, *Icarus*, 299, 84, doi: [10.1016/j.icarus.2017.07.007](https://doi.org/10.1016/j.icarus.2017.07.007)
- Harris, A. W., & D'Abramo, G. 2015, *Icarus*, 257, 302, doi: [10.1016/j.icarus.2015.05.004](https://doi.org/10.1016/j.icarus.2015.05.004)
- Harris, A. W., Fahnestock, E. G., & Pravec, P. 2009, *Icarus*, 199, 310, doi: [10.1016/j.icarus.2008.09.012](https://doi.org/10.1016/j.icarus.2008.09.012)
- Harris, A. W., & Lagerros, J. S. V. 2002, *Asteroids III*, 205
- Holmberg, J., Flynn, C., & Portinari, L. 2006, *MNRAS*, 367, 449, doi: [10.1111/j.1365-2966.2005.09832.x](https://doi.org/10.1111/j.1365-2966.2005.09832.x)
- Isaacson, P. J., Sarbadhikari, A. B., Pieters, C. M., et al. 2011, *Meteoritics and Planetary Science*, 46, 228, doi: [10.1111/j.1945-5100.2010.01148.x](https://doi.org/10.1111/j.1945-5100.2010.01148.x)
- Ivezić, Ž., Tabachnik, S., Rafikov, R., et al. 2001, *AJ*, 122, 2749, doi: [10.1086/323452](https://doi.org/10.1086/323452)
- Ivezić, Ž., Lupton, R. H., Jurić, M., et al. 2002, *AJ*, 124, 2943, doi: [10.1086/344077](https://doi.org/10.1086/344077)
- Jedicke, R., Bolin, B., Granvik, M., & Beshore, E. 2016, *Icarus*, 266, 173, doi: [10.1016/j.icarus.2015.10.021](https://doi.org/10.1016/j.icarus.2015.10.021)
- Jedicke, R., Bolin, B. T., Bottke, W. F., et al. 2018, *Frontiers in Astronomy and Space Sciences*, 5, 13, doi: [10.3389/fspas.2018.00013](https://doi.org/10.3389/fspas.2018.00013)
- Jewitt, D., Agarwal, J., Li, J., et al. 2017, *AJ*, 153, 223, doi: [10.3847/1538-3881/aa6a57](https://doi.org/10.3847/1538-3881/aa6a57)
- Jordi, K., Grebel, E. K., & Ammon, K. 2006, *A&A*, 460, 339, doi: [10.1051/0004-6361:20066082](https://doi.org/10.1051/0004-6361:20066082)
- Jorgensen, K., Rivkin, A., Binzel, R., et al. 2003, in *AAS/Division for Planetary Sciences Meeting Abstracts #35*, AAS/Division for Planetary Sciences Meeting Abstracts, 36.02
- Jurić, M., Ivezić, Ž., Lupton, R. H., et al. 2002, *AJ*, 124, 1776, doi: [10.1086/341950](https://doi.org/10.1086/341950)
- Kiefer, W. S., Macke, R. J., Britt, D. T., Irving, A. J., & Consolmagno, G. J. 2012, *Geophys. Res. Lett.*, 39, L07201, doi: [10.1029/2012GL051319](https://doi.org/10.1029/2012GL051319)
- Kwiatkowski, T., Kryszczyńska, A., Polinska, M., et al. 2008, *LPI Contributions*, 1405, 8297
- Lomb, N. R. 1976, *Ap&SS*, 39, 447, doi: [10.1007/BF00648343](https://doi.org/10.1007/BF00648343)
- Masci, F. J., Laher, R. R., Rusholme, B., et al. 2019, *PASP*, 131, 018003, doi: [10.1088/1538-3873/aae8ac](https://doi.org/10.1088/1538-3873/aae8ac)
- McMahon, J., & Scheeres, D. 2010, *Celestial Mechanics and Dynamical Astronomy*, 106, 261, doi: [10.1007/s10569-009-9247-9](https://doi.org/10.1007/s10569-009-9247-9)
- Micheli, M., Tholen, D. J., & Elliott, G. T. 2012, *NewA*, 17, 446, doi: [10.1016/j.newast.2011.11.008](https://doi.org/10.1016/j.newast.2011.11.008)
- . 2013, *Icarus*, 226, 251, doi: [10.1016/j.icarus.2013.05.032](https://doi.org/10.1016/j.icarus.2013.05.032)
- Migliorini, A., De Sanctis, M. C., Lazzaro, D., & Ammannito, E. 2017, *MNRAS*, 464, 1718, doi: [10.1093/mnras/stw2441](https://doi.org/10.1093/mnras/stw2441)
- Milani, A., Knežević, Z., Novaković, B., & Cellino, A. 2010, *Icarus*, 207, 769, doi: [10.1016/j.icarus.2009.12.022](https://doi.org/10.1016/j.icarus.2009.12.022)
- Milani, A., & Knežević, Z. 1990, *Celestial Mechanics and Dynamical Astronomy*, 49, 347, doi: [10.1007/BF00049444](https://doi.org/10.1007/BF00049444)
- Minton, D. A., Fassett, C. I., Hirabayashi, M., Howl, B. A., & Richardson, J. E. 2019, *Icarus*, 326, 63, doi: [10.1016/j.icarus.2019.02.021](https://doi.org/10.1016/j.icarus.2019.02.021)
- Mommert, M., Hora, J. L., Farnocchia, D., et al. 2014, *ApJ*, 786, 148, doi: [10.1088/0004-637X/786/2/148](https://doi.org/10.1088/0004-637X/786/2/148)
- Morais, M. H. M., & Morbidelli, A. 2002, *Icarus*, 160, 1, doi: [10.1006/icar.2002.6937](https://doi.org/10.1006/icar.2002.6937)
- Morbidelli, A., Delbo, M., Granvik, M., et al. 2020, *Icarus*, 340, 113631, doi: [10.1016/j.icarus.2020.113631](https://doi.org/10.1016/j.icarus.2020.113631)

- Moreno, F., Pozuelos, F. J., Novaković, B., et al. 2017, *ApJL*, 837, L3, doi: [10.3847/2041-8213/aa6036](https://doi.org/10.3847/2041-8213/aa6036)
- Morota, T., Haruyama, J., Miyamoto, H., et al. 2009, *Meteoritics and Planetary Science*, 44, 1115, doi: [10.1111/j.1945-5100.2009.tb01211.x](https://doi.org/10.1111/j.1945-5100.2009.tb01211.x)
- Moskovitz, N. A., Jedicke, R., Gaidos, E., et al. 2008, *Icarus*, 198, 77, doi: [10.1016/j.icarus.2008.07.006](https://doi.org/10.1016/j.icarus.2008.07.006)
- Ofek, E. O. 2012, *The Astrophysical Journal*, 749, 10
- Oke, J. B., Cohen, J. G., Carr, M., et al. 1995, *PASP*, 107, 375, doi: [10.1086/133562](https://doi.org/10.1086/133562)
- Parker, A., Ivezić, Ž., Jurić, M., et al. 2008, *Icarus*, 198, 138, doi: [10.1016/j.icarus.2008.07.002](https://doi.org/10.1016/j.icarus.2008.07.002)
- Perley, D. A. 2019, *PASP*, 131, 084503, doi: [10.1088/1538-3873/ab215d](https://doi.org/10.1088/1538-3873/ab215d)
- Press, W. H., Flannery, B. P., & Teukolsky, S. A. 1986, *Numerical recipes. The art of scientific computing*
- Pruyne, T. A., Wierzbos, K. W., D., R., Christensen, E., & Farneth, G. 2020, *Minor Planet Electronic Circulars*, 2020-D104, 104
- Raab, H. 2012, *Astrometrica: Astrometric data reduction of CCD images*. <http://ascl.net/1203.012>
- Reddy, V., Sanchez, J. A., Bottke, W. F., et al. 2016, *AJ*, 152, 162, doi: [10.3847/0004-6256/152/6/162](https://doi.org/10.3847/0004-6256/152/6/162)
- Rein, H., & Liu, S.-F. 2012, *A&A*, 537, A128, doi: [10.1051/0004-6361/201118085](https://doi.org/10.1051/0004-6361/201118085)
- Rein, H., & Spiegel, D. S. 2015, *MNRAS*, 446, 1424, doi: [10.1093/mnras/stu2164](https://doi.org/10.1093/mnras/stu2164)
- Rein, H., Hernandez, D. M., Tamayo, D., et al. 2019, *Mon. Not. R. Astron. Soc.*, 485, 5490, doi: [10.1093/mnras/stz769](https://doi.org/10.1093/mnras/stz769)
- Rockosi, C., Stover, R., Kibrick, R., et al. 2010, in *Society of Photo-Optical Instrumentation Engineers (SPIE) Conference Series*, Vol. 7735, Proc. SPIE, 77350R
- Scheirich, P., Pravec, P., Kušnirák, P., et al. 2019, *arXiv e-prints*, arXiv:1912.06456. <https://arxiv.org/abs/1912.06456>
- Schunová-Lilly, E., Jedicke, R., Vereš, P., Denneau, L., & Wainscoat, R. J. 2017, *Icarus*, 284, 114, doi: [10.1016/j.icarus.2016.11.010](https://doi.org/10.1016/j.icarus.2016.11.010)
- Shao, M., Nemati, B., Zhai, C., et al. 2014, *ApJ*, 782, 1, doi: [10.1088/0004-637X/782/1/1](https://doi.org/10.1088/0004-637X/782/1/1)
- Sidorenko, V. V., Neishtadt, A. I., Artemyev, A. V., & Zelenyi, L. M. 2014, *Celestial Mechanics and Dynamical Astronomy*, 120, 131, doi: [10.1007/s10569-014-9565-4](https://doi.org/10.1007/s10569-014-9565-4)
- Solontoi, M., Ivezić, Ž., Jurić, M., et al. 2012, *Icarus*, 218, 571, doi: [10.1016/j.icarus.2011.10.008](https://doi.org/10.1016/j.icarus.2011.10.008)
- Stellingwerf, R. F. 1978, *ApJ*, 224, 953, doi: [10.1086/156444](https://doi.org/10.1086/156444)
- Thirouin, A., Moskovitz, N., Binzel, R. P., et al. 2016, *AJ*, 152, 163, doi: [10.3847/0004-6256/152/6/163](https://doi.org/10.3847/0004-6256/152/6/163)
- Tingay, S. J., Kaplan, D. L., McKinley, B., et al. 2013, *AJ*, 146, 103, doi: [10.1088/0004-6256/146/4/103](https://doi.org/10.1088/0004-6256/146/4/103)
- Tonry, J. L., Stubbs, C. W., Lykke, K. R., et al. 2012, *ApJ*, 750, 99, doi: [10.1088/0004-637X/750/2/99](https://doi.org/10.1088/0004-637X/750/2/99)
- Urrutxua, H., & Bombardelli, C. 2017
- Vereš, P., Jedicke, R., Fitzsimmons, A., et al. 2015, *Icarus*, 261, 34, doi: [10.1016/j.icarus.2015.08.007](https://doi.org/10.1016/j.icarus.2015.08.007)
- Vereš, P., & Chesley, S. R. 2017, *AJ*, 154, 12, doi: [10.3847/1538-3881/aa73d1](https://doi.org/10.3847/1538-3881/aa73d1)
- Vokrouhlický, D., Bottke, W. F., Chesley, S. R., Scheeres, D. J., & Statler, T. S. 2015, *Asteroids IV*, 509, doi: [10.2458/azu_uapress_9780816530595-ch027](https://doi.org/10.2458/azu_uapress_9780816530595-ch027)
- Vokrouhlický, D., Pravec, P., Durech, J., et al. 2017, *A&A*, 598, A91, doi: [10.1051/0004-6361/201629670](https://doi.org/10.1051/0004-6361/201629670)
- Walsh, K. J., Richardson, D. C., & Michel, P. 2008, *Nature*, 454, 188, doi: [10.1038/nature07078](https://doi.org/10.1038/nature07078)
- Warner, B. D., Harris, A. W., & Pravec, P. 2009, *Icarus*, 202, 134, doi: [10.1016/j.icarus.2009.02.003](https://doi.org/10.1016/j.icarus.2009.02.003)
- Wisdom, J. 1983, *Icarus*, 56, 51, doi: [10.1016/0019-1035\(83\)90127-6](https://doi.org/10.1016/0019-1035(83)90127-6)
- Ye, Q., Masci, F. J., Lin, H. W., et al. 2019a, *PASP*, 131, doi: [10.1088/1538-3873/ab1b18](https://doi.org/10.1088/1538-3873/ab1b18)
- Ye, Q., Kelley, M. S. P., Bodewits, D., et al. 2019b, *ApJL*, 874, L16, doi: [10.3847/2041-8213/ab0f3c](https://doi.org/10.3847/2041-8213/ab0f3c)
- Ye, Q., Kelley, M. S. P., Bolin, B. T., et al. 2020, *AJ*, 159, 77, doi: [10.3847/1538-3881/ab659b](https://doi.org/10.3847/1538-3881/ab659b)
- Zappala, V., Cellino, A., Barucci, A. M., Fulchignoni, M., & Lupishko, D. F. 1990, *A&A*, 231, 548

Zhai, C., Ye, Q., Shao, M., et al. 2020, PASP, 132,
064502, doi: [10.1088/1538-3873/ab828b](https://doi.org/10.1088/1538-3873/ab828b)

Table 1. Summary of 2020 CD₃ photometry taken on 2020 March 23 UTC.

Date ¹ (MJD UTC)	Filter ²	Exp ³ (s)	H^4
58931.5452386	R	60 s	31.39 ± 0.11
58931.5456206	g	120 s	31.91 ± 0.17
58931.5465002	R	60 s	32.33 ± 0.17
58931.5477386	R	60 s	32.11 ± 0.16
58931.5484447	g	120 s	32.13 ± 0.21
58931.5489424	R	30 s	32.00 ± 0.13
58931.5498336	R	30 s	31.50 ± 0.2
58931.5520674	B	120 s	31.90 ± 0.12
58931.5544632	B	120 s	32.35 ± 0.15
58931.5599146	B	120 s	31.94 ± 0.12
58931.5617317	B	120 s	31.89 ± 0.11
58931.5643474	g	120 s	31.36 ± 0.11
58931.566153	g	120 s	32.02 ± 0.19
58931.5730511	V	120 s	31.80 ± 0.12
58931.5749956	V	120 s	32.08 ± 0.16
58931.5788613	V	120 s	31.90 ± 0.14

Table 1. Columns: (1) observation date correct for light travel time; (2) Keck I/LRIS Filter; (3) Exposure time (4) V band equivalent H magnitude with 1 σ uncertainties

Table 2. Summary of astrometry from observations taken by Keck I/LRIS and other observatories between 2020 February 15 UTC and 2020 March 23 UTC.

Date ¹ (UTC)	R.A. ²	Dec. ³	$\sigma_{\text{R.A.}}$ ⁴ ($''$)	$\sigma_{\text{Dec.}}$ ⁵ ($''$)	$X_{\text{res.}}$ ⁶ ($''$)	$Y_{\text{res.}}$ ⁷ ($''$)	Obs. code ⁸
2020 Feb 15.511140	13 03 33.110	+09 10 43.10	1.00	1.00	-0.33	-0.02	G96
2020 Feb 15.516240	13 03 34.520	+09 13 03.60	1.00	1.00	+0.07	+0.59	G96
2020 Feb 15.521330	13 03 35.960	+09 15 21.90	1.00	1.00	-0.50	+0.47	G96
2020 Feb 15.545470	13 03 44.540	+09 26 01.30	1.00	1.00	-0.17	-0.78	G96
2020 Feb 15.545640	13 03 44.640	+09 26 05.90	1.00	1.00	+0.27	-0.60	G96
2020 Feb 15.545820	13 03 44.700	+09 26 11.10	1.00	1.00	+0.06	-0.08	G96
2020 Feb 15.545990	13 03 44.770	+09 26 15.40	1.00	1.00	+0.05	-0.20	G96
2020 Feb 15.995517	13 18 35.410	+12 12 02.10	1.00	1.00	-0.36	+0.15	L01
2020 Feb 15.997407	13 18 36.130	+12 12 45.40	1.00	1.00	+0.05	+0.38	L01
2020 Feb 15.999831	13 18 36.990	+12 13 40.90	1.00	1.00	+0.02	+0.80	L01
2020 Feb 16.004013	13 18 38.390	+12 15 14.70	1.00	1.00	-0.30	-0.03	L01
2020 Feb 16.005639	13 18 38.940	+12 15 51.70	1.00	1.00	-0.02	+0.31	L01
2020 Feb 16.363950	13 25 20.450	+14 16 52.80	1.00	1.00	+0.26	+0.52	291
2020 Feb 16.366530	13 25 20.430	+14 17 41.60	1.00	1.00	+0.17	+0.61	291
2020 Feb 16.369160	13 25 20.380	+14 18 30.70	1.00	1.00	+0.09	+0.26	291
2020 Feb 16.437910	13 25 08.050	+14 38 18.00	1.00	1.00	+0.14	+0.05	I52
2020 Feb 16.439840	13 25 07.630	+14 38 49.70	1.00	1.00	+0.02	+0.18	I52
2020 Feb 16.441770	13 25 07.230	+14 39 20.80	1.00	1.00	+0.25	-0.15	I52
2020 Feb 16.443700	13 25 06.810	+14 39 52.00	1.00	1.00	+0.23	-0.25	I52
2020 Feb 17.040534	13 34 23.090	+16 43 52.20	1.00	1.00	+1.20	+0.32	L01
2020 Feb 17.046622	13 34 22.810	+16 45 14.60	1.00	1.00	-0.06	-0.01	L01
2020 Feb 17.051069	13 34 43.300	+16 40 45.90	0.80	0.80	-0.21	-0.02	J95
2020 Feb 17.054297	13 34 22.440	+16 46 58.00	1.00	1.00	+0.04	+0.44	L01
2020 Feb 17.070077	13 34 45.600	+16 45 07.30	0.80	0.80	+0.06	-0.33	J95
2020 Feb 17.084942	13 34 46.670	+16 48 26.90	0.80	0.80	-0.13	-0.01	J95
2020 Feb 17.100726	13 34 47.270	+16 51 52.70	0.80	0.80	+0.07	-0.36	J95
2020 Feb 17.508000	13 38 02.170	+18 18 19.10	1.00	1.00	+0.37	+0.61	G96
2020 Feb 17.510030	13 38 01.600	+18 18 36.30	1.00	1.00	+0.82	+0.12	G96
2020 Feb 17.512060	13 38 00.990	+18 18 54.50	1.00	1.00	+0.60	+0.76	G96
2020 Feb 17.514090	13 38 00.380	+18 19 11.50	1.00	1.00	+0.28	+0.32	G96
2020 Feb 17.980051	13 45 25.930	+19 19 39.42	1.00	1.00	-0.89	+0.35	Z84
2020 Feb 17.998253	13 45 29.233	+19 23 16.64	1.00	1.00	-0.80	-0.04	Z84
2020 Feb 18.016457	13 45 30.942	+19 26 49.53	1.00	1.00	-0.79	-0.11	Z84
2020 Feb 18.414650	13 47 52.480	+20 25 18.00	1.00	1.00	+0.09	+0.40	G96
2020 Feb 18.415230	13 47 52.300	+20 25 23.20	1.00	1.00	+0.17	+0.51	G96

Continued on next page

Table 2 – *Continued from previous page*

Date ¹ (UTC)	R.A. ²	Dec. ³	$\sigma_{\text{R.A.}}$ ⁴ (")	$\sigma_{\text{Dec.}}$ ⁵ (")	$X_{\text{res.}}$ ⁶ (")	$Y_{\text{res.}}$ ⁷ (")	Obs. code ⁸
2020 Feb 18.415810	13 47 52.140	+20 25 27.20	1.00	1.00	+0.54	-0.57	G96
2020 Feb 18.416390	13 47 51.930	+20 25 33.00	1.00	1.00	+0.21	+0.16	G96
2020 Feb 19.301670	13 55 16.820	+21 55 58.10	1.00	1.00	-0.51	+0.82	G96
2020 Feb 19.303920	13 55 16.910	+21 56 17.50	1.00	1.00	+0.23	-0.70	G96
2020 Feb 19.306180	13 55 16.960	+21 56 39.00	1.00	1.00	+0.71	-0.15	G96
2020 Feb 20.418810	14 00 29.620	+23 35 56.90	1.00	1.00	-0.02	+0.59	G96
2020 Feb 20.419560	14 00 29.390	+23 36 00.70	1.00	1.00	+0.44	-0.01	G96
2020 Feb 20.420320	14 00 29.140	+23 36 05.20	1.00	1.00	+0.69	+0.05	G96
2020 Feb 20.421070	14 00 28.880	+23 36 11.00	1.00	1.00	+0.76	+0.97	G96
2020 Feb 21.095901	14 03 49.976	+24 21 03.47	1.00	1.00	-0.39	-0.35	Z84
2020 Feb 21.120492	14 03 42.513	+24 23 16.74	1.00	1.00	-0.47	-0.68	Z84
2020 Feb 21.146268	14 03 33.897	+24 25 23.50	1.00	1.00	+0.03	-0.04	Z84
2020 Feb 21.172268	14 03 24.721	+24 27 15.50	1.00	1.00	+0.09	-0.23	Z84
2020 Feb 21.196581	14 03 16.142	+24 28 46.33	1.00	1.00	+0.54	-0.46	Z84
2020 Feb 27.642330	14 19 58.612	+29 10 39.85	0.40	0.40	+0.00	+0.01	T14
2020 Feb 27.643742	14 19 58.040	+29 10 40.82	0.40	0.40	-0.01	+0.01	T14
2020 Feb 27.645156	14 19 57.468	+29 10 41.76	0.40	0.40	-0.04	+0.02	T14
2020 Mar 01.477510	14 23 44.930	+30 15 25.40	1.00	1.00	+0.40	-0.33	G37
2020 Mar 01.479210	14 23 44.270	+30 15 27.40	1.00	1.00	-0.36	-0.14	G37
2020 Mar 01.480250	14 23 43.970	+30 15 28.30	1.00	1.00	+0.52	-0.32	G37
2020 Mar 22.483420	14 21 40.530	+33 16 25.12	0.40	0.40	-0.04	+0.00	T14
2020 Mar 22.487379	14 21 38.999	+33 16 27.56	0.40	0.40	+0.03	+0.01	T14
2020 Mar 23.544957	14 20 00.300	+33 15 49.70	1.00	1.00	+0.03	+0.01	568
2020 Mar 23.548839	14 19 58.780	+33 15 48.50	1.00	1.00	-0.10	-0.13	568
2020 Mar 23.549729	14 19 58.420	+33 15 47.90	1.00	1.00	+0.28	+0.13	568

Table 2. Columns: (1) UTC observation date at the mid-point of the exposure; (2) right ascension; (3) declination; (4) uncertainty in right ascension; (5) uncertainty in declination; (6) observed-minus-computed residual in the X direction; (7) observed-minus-computed residual in the Y direction; (8) Minor Planet Center Observatory Code

Table 3. Orbital elements of 2020 AV₂ based on observations collected between 2020 February 15 UTC and 2020 March 23 UTC. The orbital elements are shown for the Julian date (JD) shown using the software `Find_Orb` by Bill Gray. The 1 σ uncertainties are given in parentheses.

Heliocentric Elements	
Epoch (JD)	2,458,931.5
Time of perihelion, T_p (JD)	2,458,907.045 \pm (0.019)
Semi-major axis, a (au)	1.01713 \pm (6.49x10 ⁻⁷)
Eccentricity, e	0.02858 \pm (6.58x10 ⁻⁷)
Perihelion, q (au)	0.98806 \pm (6.51x10 ⁻⁸)
Aphelion, Q (au)	1.04620 \pm (1.34x10 ⁻⁶)
Inclination, i ($^\circ$)	0.55483 \pm (1.80x10 ⁻⁵)
Ascending node, Ω ($^\circ$)	116.954 \pm (1.70x10 ⁻³)
Argument of perihelion, ω ($^\circ$)	357.557 \pm (1.30x10 ⁻³)
Mean Anomaly, M ($^\circ$)	65.1632 \pm (4.44x10 ⁻⁴)
Geocentric Elements	
Epoch (JD)	2,458,931.5
Time of perihelion, $T_{p,g}$ (JD)	2,458,893.615 \pm (7.47x10 ⁻⁵)
Semi-major axis, a_g (au)	0.00752 \pm (3.72x10 ⁻⁷)
Eccentricity, e_g	0.95821 \pm (9.88x10 ⁻⁷)
Perihelion, q_g (au)	0.00031 \pm (2.05x10 ⁻⁸)
Aphelion, Q_g (au)	0.01472 \pm (7.24x10 ⁻⁷)
Inclination, i_g ($^\circ$)	146.68615 \pm (7.24x10 ⁻⁷)
Ascending node, Ω_g ($^\circ$)	309.888 \pm (5.5x10 ⁻⁴)
Argument of perihelion, ω_g ($^\circ$)	280.529 \pm (1.0x10 ⁻³)
Mean Anomaly, M_g ($^\circ$)	99.299 \pm (7.0x10 ⁻³)
Area-to-Mass ratio, AMR (m ² /kg)	6.96x10 ⁻⁴ \pm (2.41x10 ⁻⁴)
Absolute Magnitude, H	31.9 \pm (0.1)